

Variational multiscale enrichment method with mixed boundary conditions for elasto-viscoplastic problems

Shuhai Zhang* and Caglar Oskay†

Department of Civil and Environmental Engineering
Vanderbilt University
Nashville, TN 37235

Abstract

This manuscript presents the formulation and implementation of the variational multiscale enrichment (VME) method for the analysis of elasto-viscoplastic problems. VME is a global-local approach that allows accurate fine scale representation at small subdomains, where important physical phenomena are likely to occur. The response within far-fields is idealized using a coarse scale representation. The fine scale representation not only approximates the coarse grid residual, but also accounts for the material heterogeneity. A one-parameter family of mixed boundary conditions that range from Dirichlet to Neumann is employed to study the effect of the choice of the boundary conditions at the fine scale on accuracy. The inelastic material behavior is modeled using Perzyna type viscoplasticity coupled with flow stress evolution idealized by the Johnson-Cook model. Numerical verifications are performed to assess the performance of the proposed approach against the direct finite element simulations. The results of verification studies demonstrate that VME with proper boundary conditions accurately model the inelastic response accounting for material heterogeneity.

Keywords: Multiscale modeling, Variational multiscale enrichment; Elasto-viscoplastic; Global-local modeling.

1 Introduction

Environment exposure induced deterioration of mechanical properties and related structural failures have been a difficult problem to address from both physical and computational perspec-

*Department of Civil and Environmental Engineering, Vanderbilt University, Nashville, TN 37235, United States. Email: shuhai.zhang@vanderbilt.edu

†Corresponding author address: VU Station B#351831, 2301 Vanderbilt Place, Nashville, TN 37235. Email: caglar.oskay@vanderbilt.edu

tives. The problem is quite pervasive ranging from stress corrosion to hydrogen embrittlement and oxidation of metals to sulfate and chloride attack in concrete and hydration induced leaching in polymers. In surface degradation problems, an aggressive environmental agent attacks the surface of the structure inducing property changes such as embrittlement, cracking and reduction of monotonic and cyclic strength and life as a consequence. The property changes could be due to phase transformation activated by the diffusing agent or lattice strains due to elevated concentrations and pile-ups around the lattice imperfections.

In certain problems, the structural property degradation is severe even for a very small thickness of affected region. For instance, titanium alloys, which are candidate structural materials for hypersonic aircraft, are subjected to formation of a brittle case of oxygen rich layer on its surface under the severe thermo-mechanical environment. While the brittle case is of the order of a few tens of microns thick, the presence of acoustic loads threaten micron cracks within the brittle case to rapidly propagate and cause structural failure. From the computational perspective, this calls for a very refined analysis around exposed surfaces. In order to retain computational tractability, the refinement cannot be extended to the entire structure.

Global-local numerical approaches are well-suited to address such problems. These methods attempt to capture the fine scale behavior at small subdomains of the problem, whereas a coarse discretization and modeling is used to approximate the behavior in the remainder of the problem domain. Starting from the early works of Mote [28], a number of global local methods have been proposed including the global-local finite element method [29, 24, 10, 14], the S-version finite element method [9], the domain decomposition method [23], the generalized finite element method [8], Multiscale coupling based on Lagrange multiplier method [25], among others. Hughes and coworkers [17, 19] proposed the variational multiscale method (VMM), which allows the incorporation of fine scale response to an otherwise coarse representation. VMM is based on the additive decomposition of the response field into coarse and fine components. The coarse component of the response is evaluated based on a coarse grid. The fine scale response is evaluated either semi-analytically through variational projection [13, 18] or numerically, by directly solving for the residual response using a fine grid. Strictly speaking, the former does not have a global-local character since the fine scale response remains unresolved. The latter gives rise to the numerical subgrid upscaling method [1, 2] or the variational multiscale enrichment (VME) method [30, 31].

The numerical subgrid upscaling and variational multiscale enrichment methods have been proposed to investigate both flow and deformation problems. Arbogast [1] formulated a subgrid upscaling scheme for locally conservative porous media flow. The evaluation procedure was based on the construction of the fine scale response field using numerical Green's functions, which provides a reduced approximation basis to an otherwise computationally complex

fine scale problem. The fine scale response was evaluated based on the homogeneous Dirichlet boundary conditions originally proposed in Refs. [3, 5] similar to residual-free bubble functions for approximating the fine scale residual. Juanes and Dub [21] employed the numerical subgrid upscaling scheme with a relaxed subgrid boundary constraint to solve porous media flow problems. Garikipati and Hughes [13] extended the VMM approach to address strain localization problems in the presence of plastic deformations. This method employed the variational projection method, instead of numerical evaluation of the fine scale response. Garikipati [11] incorporated fine scale strain gradient theories into the variational multiscale continuum formulation. With naturally derived stability tensors, Masud and Xia [26] developed a stabilized mixed finite element method for VMM. Yeon and Youn [38] performed variational multiscale analysis on the elastoplastic deformation problem using a meshfree method. Hund and Ramm [20] employed a continuum damage mechanics model in the context of the numerical subgrid upscaling scheme to address the strain localization problem. They investigated the effect of fine scale boundary constraint based on the Lagrange multiplier method of Markovic and Ibrahimbegovic [25] as well as the penalty method. More recently, Oskay [30] proposed the VME method, which also exhibits global-local character. In this approach, the subgrids are allowed to be heterogeneous and the approach was extended to coupled transport-deformation problems. The effect of a class of boundary conditions ranging from homogeneous Dirichlet to Neumann on accuracy was investigated in Ref. [31] in the context of diffusion and elastic deformation problems.

Other approaches, such as the multiscale projection method proposed by Qian et al. [34], also rely on the additive decomposition of the displacement field. Similar to VMM, this approach employs projection operators to couple the fine and coarse scale response fields, and were used to investigate problems that involve atomistic-to-continuum coupling. Furthermore, the microscale boundary conditions enforced in the multiscale projection method is of Dirichlet type computed from the coarse scale response. In contrast, the present approach relies on the variational arguments to couple the fine and coarse response directly and employ a mixed boundary condition for the microscale problem as described below. Another alternative approach to solve a coupled local-global problem is through preconditioning of the linear system at each nonlinear iteration [4, 16, 35]. While this approach relies on the resolution of the microstructural heterogeneity in the problem domain, it also has several advantages particularly in view of the availability of powerful multigrid and other iterative solvers (e.g. GMRES).

The current manuscript extends the capabilities of the variational multiscale enrichment method to address inelastic material behavior in the context of deformation problems. The novel contributions of the manuscript are: (1) The VME approach is formulated for elasto-viscoplastic material behavior: the previous work on VME included only elastic material behavior; and (2) the performance of the inelastic VME formulation was assessed as a function of

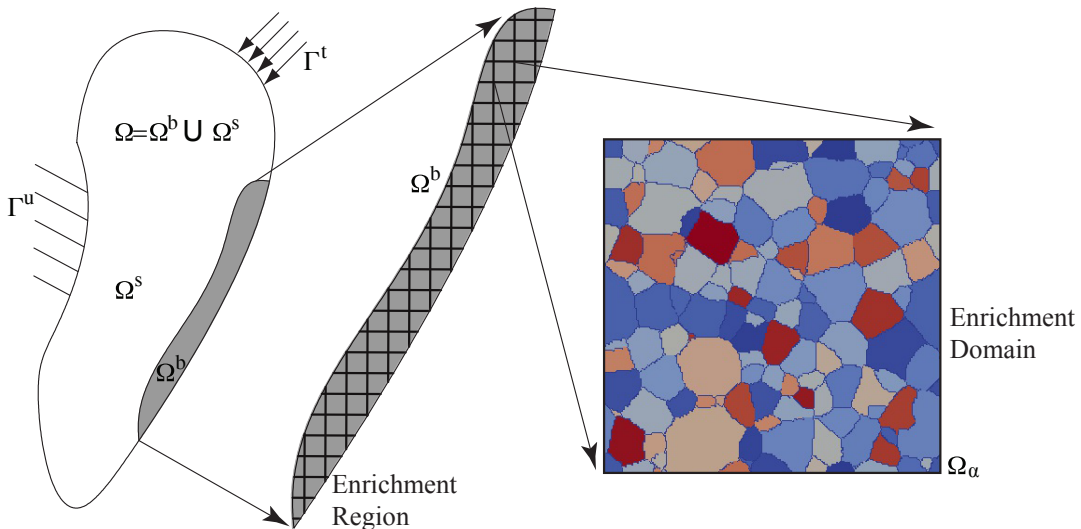


Figure 1: The schematic representation of the overall problem domain, enrichment region and an enrichment domain.

the choice of boundary conditions proposed in Ref. [31] in the viscoplastic regime. In the proposed approach, the fine scale representation not only approximates the coarse grid residual, but also accounts for the material heterogeneity. A one-parameter family of mixed boundary conditions that range from Dirichlet to Neumann is employed to study the effect of the choice of the boundary conditions at the fine scale on accuracy. The inelastic material behavior is modeled using Perzyna type viscoplasticity coupled with flow stress evolution idealized by the Johnson-Cook model. Numerical verifications are performed to assess the performance of the proposed approach against the direct finite element simulations. The results of verification studies demonstrate that VME with proper boundary conditions accurately model the inelastic response accounting for material heterogeneity.

The remainder of this manuscript is organized as the follows: Section 2 provides the problem statement and governing equations of the boundary value problems. Section 3 details the variational multiscale enrichment methodology for solving inelastic mechanical problems with elasto-viscoplastic material model. Section 4 describes the computational implementation of the proposed methodology, including finite element discretization of the problems and the solution strategy. Numerical experiments are provided in Section 5, including the effect of boundary conditions on accuracy of the proposed computational framework. Section 6 presents conclusions and future research directions.

2 Governing Equations

We start by defining the governing equations that idealize the inelastic deformation within the problem domain. Let $\Omega \subset \mathbb{R}^{n_{sd}}$ be the domain of the structure as illustrated in Fig. 1, where

n_{sd} is the number of spatial dimensions. The equilibrium equation is expressed as:

$$\nabla \cdot \boldsymbol{\sigma}(\mathbf{x}, t) = 0; \quad \mathbf{x} \in \Omega, \quad t \in [0, t_o] \quad (1)$$

in the absence of the body forces. \mathbf{x} and t respectively denote the position and time coordinates; $\boldsymbol{\sigma}$ is the stress tensor; ∇ the gradient operator; (\cdot) the inner product; and t_o is the end of the observation period. The boundary conditions are given as:

$$\text{Dirichlet B.C.:} \quad \mathbf{u}(\mathbf{x}, t) = \tilde{\mathbf{u}}(\mathbf{x}, t); \quad \mathbf{x} \in \Gamma^u \quad (2)$$

$$\text{Neumann B.C.:} \quad \boldsymbol{\sigma}(\mathbf{x}, t) \cdot \mathbf{n} = \tilde{\mathbf{t}}(\mathbf{x}, t); \quad \mathbf{x} \in \Gamma^t \quad (3)$$

where, $\tilde{\mathbf{u}}$ is the prescribed displacement along the boundary subdomain, Γ^u ; $\tilde{\mathbf{t}}$ the prescribed traction along the boundary subdomain, Γ^t . The decomposition of the external boundary is such that $\Gamma = \Gamma^u \cup \Gamma^t$ and $\Gamma^u \cap \Gamma^t \equiv \emptyset$.

The description of the constitutive relationship over the parts of the domain that remain unresolved, as well as the parts that resolve the micro-heterogeneity is taken to be elasto-viscoplastic. The constitutive equation is expressed in the rate form as:

$$\dot{\boldsymbol{\sigma}}(\mathbf{x}, t) = \mathbf{L}(\mathbf{x}, t) : [\dot{\boldsymbol{\varepsilon}}(\mathbf{x}, t) - \dot{\boldsymbol{\varepsilon}}^{vp}(\mathbf{x}, t)] \quad (4)$$

in which, \mathbf{L} is the tensor of elastic moduli; $\boldsymbol{\varepsilon}$ and $\boldsymbol{\varepsilon}^{vp}$ denote total strain and viscoplastic strain tensors, respectively. The superposed dot indicates material time derivative and $(:)$ the double inner product. The evolution of the viscoplastic strain is idealized based on the Perzyna's viscoplastic model [33, 36, 37]:

$$\dot{\boldsymbol{\varepsilon}}^{vp} = \gamma \left\langle \frac{f}{\sigma_y} \right\rangle^q \frac{\partial f}{\partial \boldsymbol{\sigma}} \quad (5)$$

where, σ_y denotes the flow stress; γ the fluidity parameter; q the viscoplastic hardening exponent; $\langle \cdot \rangle$ the Macaulay brackets (i.e., $\langle \cdot \rangle = ((\cdot) + |\cdot|)/2$); and f the loading function defined based on the classical J_2 plasticity:

$$f(\boldsymbol{\sigma}, \boldsymbol{\varepsilon}^{vp}) = \sqrt{3}\bar{\sigma} - \sigma_y(\bar{\boldsymbol{\varepsilon}}^{vp}) \quad (6)$$

in which, $\bar{\sigma}$ denotes the second invariant of the deviatoric stress tensor, $\mathbf{s} = \boldsymbol{\sigma} - \text{tr}(\boldsymbol{\sigma})\boldsymbol{\delta}/3$; $\text{tr}(\cdot)$ the trace operator; $\boldsymbol{\delta}$ the Kronecker delta; and $\bar{\boldsymbol{\varepsilon}}^{vp}$ is the effective viscoplastic strain defined as:

$$\bar{\boldsymbol{\varepsilon}}^{vp} = \sqrt{\frac{2}{3} \boldsymbol{\varepsilon}^{vp} : \boldsymbol{\varepsilon}^{vp}} \quad (7)$$

The flow stress is a function of the effective viscoplastic strain using a reduced version of the

Johnson-Cook model:

$$\sigma_y = A + B(\bar{\varepsilon}^{vp})^n \quad (8)$$

where, A, B and n are material parameters. We note that the standard Johnson-Cook model includes the effect of strain rate and temperature into the flow equation. The strain rate effect is modeled directly using the Perzyna formulation and the temperature dependence is suppressed for simplicity.

Equations (1)-(8) constitute the strong form equations of the elasto-viscoplastic problem. The proposed enrichment approach operates within a variational setting. The equilibrium equation along with the boundary conditions is expressed in the weak form as follows:

Find $\mathbf{u} \in \mathcal{V} \times [0, t_o]$ such that:

$$\int_{\Omega} \nabla \mathbf{w} : \boldsymbol{\sigma}(\mathbf{x}, t) \, d\Omega - \int_{\Gamma^t} \mathbf{w} \cdot \tilde{\mathbf{t}}(\mathbf{x}, t) \, d\Gamma = 0; \quad \forall \mathbf{w} \in [H_0^1(\Omega)]^{n_{sd}} \quad (9)$$

along with the constitutive equations (i.e., Eqs. (4)-(8)) that relate the displacement field to the stress field. The trial space for the displacement field is:

$$\mathcal{V} \equiv \{ \hat{\mathbf{u}} \in [H^1(\Omega)]^{n_{sd}} \mid \hat{\mathbf{u}} = \tilde{\mathbf{u}} \text{ on } \mathbf{x} \in \Gamma^u \} \quad (10)$$

in which, \mathbf{w} is the test function; $H^1(\Omega)$ is the Sobolev space of functions with square integrable values and derivatives defined in the domain, Ω ; $H_0^1(\Omega)$ is the subspace of functions in $H^1(\Omega)$ and that are homogeneous along the domain boundary, Γ .

3 Variational Multiscale Enrichment

The governing equations (Eqs. (1)-(8)) are evaluated using the variational multiscale enrichment method. In this approach, the problem domain, Ω , is decomposed into two non-overlapping subdomains, as demonstrated in Fig. 1:

$$\Omega \equiv \Omega^s \cup \Omega^b; \quad \Omega^s \cap \Omega^b \equiv \emptyset \quad (11)$$

where, Ω^b denotes the enrichment region, in which the response is accurately characterized by modeling and resolving at the scale of microstructural heterogeneities. In the substrate region Ω^s , coarse scale modeling is taken to be sufficient to accurately capture the mechanical response. It is implicitly assumed that the domain is large enough to computationally prohibit full resolution of the microscale heterogeneities throughout the structure. The enrichment region is further partitioned into enrichment (microstructural) domains. The partitioning is done such that the resulting enrichment domains are simple such that they can be represented

by a single finite element at the coarse scale:

$$\Omega^b = \bigcup_{\alpha=1}^{n_{\text{en}}} \Omega_\alpha; \quad \Omega_\alpha \cap \Omega_\beta \equiv \emptyset \quad \text{when } \alpha \neq \beta \quad (12)$$

where, n_{en} denotes the total number of enrichment domains. Within each enrichment domain, the microscale heterogeneity is resolved and numerically evaluated.

The boundary of an enrichment domain, α , can be decomposed into the following components:

$$\Gamma_\alpha \equiv \partial\Omega_\alpha = \Gamma_\alpha^{\text{int}} \cup \Gamma_\alpha^s \cup \Gamma_\alpha^u \cup \Gamma_\alpha^t \quad (13)$$

in which, Γ_α^s is the part of the boundary that intersects with the substrate region boundary ($\Gamma_\alpha^s \equiv \Gamma_\alpha \cap \partial\Omega^s$); Γ_α^u is the part of the boundary that intersects with the Dirichlet boundary of the problem domain ($\Gamma_\alpha^u \equiv \Gamma_\alpha \cap \Gamma^u$); Γ_α^t is the part of the boundary that intersects with the Neumann boundary of the problem domain ($\Gamma_\alpha^t \equiv \Gamma_\alpha \cap \Gamma^t$); and, $\Gamma_\alpha^{\text{int}}$ is the inter-enrichment domain boundaries:

$$\Gamma_\alpha^{\text{int}} \equiv \bigcup_{\beta \in I_\alpha} \Gamma_\alpha^\beta \quad (14)$$

where the neighbor index set of enrichment domain Ω_α , can be expressed as: $I_\alpha \equiv \{\beta \leq n_{\text{en}} \mid \Gamma_{\alpha\beta} \neq \emptyset\}$; $\Gamma_{\alpha\beta}$ is the inter-enrichment domain boundary between α and β domain ($\Gamma_{\alpha\beta} \equiv \Gamma_\alpha \cap \Gamma_\beta$); Γ_α^β and Γ_β^α denotes the α and β side of the inter-enrichment domain boundary, respectively.

The displacement response field is decomposed into macroscale and microscale contributions through additive two-scale decomposition:

$$\mathbf{u}(\mathbf{x}, t) = \mathbf{u}^M(\mathbf{x}, t) + \sum_{\alpha=1}^{n_{\text{en}}} \mathcal{H}(\Omega_\alpha) \mathbf{u}_\alpha^m(\mathbf{x}, t) \quad (15)$$

where, superscripts M and m denote the macroscale and microscale response fields, respectively, and

$$\mathcal{H}(\Omega_\alpha) = \begin{cases} 1, & \text{if } \mathbf{x} \in \Omega_\alpha \\ 0, & \text{elsewhere} \end{cases} \quad (16)$$

Equation (16) ensures that the microscale displacement field, \mathbf{u}_α^m , is nonzero only on the closure of enrichment domain, Ω_α . The decomposition of the displacement field is performed such that the corresponding function spaces recover the trial function space through direct sum ($\mathbf{u}^M \in \mathcal{V}^M(\Omega)$ and $\mathbf{u}_\alpha^m \in \mathcal{V}_\alpha(\Omega_\alpha)$):

$$\mathcal{V}(\Omega) = \mathcal{V}^M(\Omega) \oplus \bigoplus_{\alpha=1}^{n_{\text{en}}} \mathcal{V}_\alpha(\Omega_\alpha) \quad (17)$$

in which, $\mathcal{V}^M(\Omega) \subset [H^1(\Omega)]^{n_{sd}}$ is the trial space for the macroscale displacement field and $\mathcal{V}_\alpha(\Omega_\alpha) \subset [H^1(\Omega_\alpha)]^{n_{sd}}$ is the trial space for the microscale displacement field within enrichment domain, Ω_α . This decomposition implies linear independence of the macroscale and the microscale subspaces necessary for uniqueness and stability of the numerical solution [19, 12]. Similar to Eq. (17), the test function is additively decomposed into macroscale and microscale components

$$\mathbf{w} = \mathbf{w}^M + \sum_{\alpha=1}^{n_{en}} \mathcal{H}(\Omega_\alpha) \mathbf{w}_\alpha^m \quad (18)$$

where, $\mathbf{w}^M \in \mathcal{W}^M(\Omega) \subset [H_0^1(\Omega)]^{n_{sd}}$ is the macroscale test function; and $\mathbf{w}_\alpha^m \in \mathcal{W}_\alpha(\Omega_\alpha) \subset [H^1(\Omega_\alpha)]^{n_{sd}}$ is the microscale test function of the enrichment domain, Ω_α .

Substituting Eqs.(18) and (15) into Eq. (9), the weak form of the problem yields:

$$\int_{\Omega_s} \mathbf{w}^M \cdot [\nabla \cdot \boldsymbol{\sigma}(\mathbf{u}^M, \mathbf{0})] d\Omega + \sum_{\alpha=1}^{n_{en}} \int_{\Omega_\alpha} (\mathbf{w}^M + \mathbf{w}_\alpha^m) \cdot [\nabla \cdot \boldsymbol{\sigma}(\mathbf{u}^M, \mathbf{u}_\alpha^m)] d\Omega = 0 \quad (19)$$

On the substrate domain, the stress field is determined solely from the macroscale displacement field, whereas within the enrichment region, both the macroscale and microscale displacement fields define stress. Since \mathbf{w}^M and \mathbf{w}_α^m are arbitrary and independent, a macroscale and a series of microscale problems over each enrichment domain ($\alpha = 1, 2, \dots, n_{en}$) are obtained by collecting the terms with \mathbf{w}^M and \mathbf{w}_α^m . Considering the decomposition of the boundaries in Eq. (13) and setting the microscale test functions to zero yields the weak form of the macroscale problem:

$$\int_{\Omega} \nabla \mathbf{w}^M : \boldsymbol{\sigma}(\mathbf{u}^M, \mathbf{u}_\alpha^m) d\Omega - \int_{\Gamma^t} \mathbf{w}^M \cdot \tilde{\mathbf{t}} d\Gamma - \int_{\Gamma_{sb}} \mathbf{w}^M \cdot \mathbf{t}^r d\Gamma = 0 \quad (20)$$

where, \mathbf{t}^r denotes the residual tractions along the substrate-enrichment region boundary, Γ_{sb} . The weak form of the microscale problem at an arbitrary enrichment domain, α , is obtained similarly by considering vanishing macroscale test functions:

$$\int_{\Omega_\alpha} \nabla \mathbf{w}_\alpha^m : \boldsymbol{\sigma}(\mathbf{u}^M, \mathbf{u}_\alpha^m) d\Omega - \int_{\Gamma_\alpha^t} \mathbf{w}_\alpha^m \cdot \tilde{\mathbf{t}} d\Gamma - \int_{\Gamma_\alpha \setminus \Gamma} \mathbf{w}_\alpha^m \cdot \mathbf{t} d\Gamma = 0 \quad (21)$$

in which, \mathbf{t} denotes the internal tractions along the boundaries of the enrichment domain that does not overlap with the external boundaries.

Remark 1. The residual traction along the substrate-enrichment region is:

$$\mathbf{t}^r(\mathbf{x}, t) = \mathbf{t}(\mathbf{x}, t) - \mathbf{t}^M(\mathbf{x}, t) \quad (22)$$

where, $\mathbf{t}^M = \boldsymbol{\sigma}(\mathbf{u}^M, \mathbf{0}) \cdot \mathbf{n}$ is the coarse scale component of the internal traction. The residual traction along the substrate side of the boundary is zero since the microscale response is

not resolved: i.e., $\mathbf{t}^M = \mathbf{t}$. On the enrichment side, the residual traction is non-zero and induced by the presence of microscale deformation. The inclusion of the boundary term ensures that the traction continuity is satisfied. Similar to the finite element method, the traction continuity is weakly enforced. Along all neighboring enrichment domain boundaries, the fine scale component of the response is resolved on either side and hence taken to be weakly satisfied. When non-conforming meshes are used, the traction continuity needs to be explicitly enforced on the neighboring enrichment domain boundaries as well.

3.1 Mixed boundary conditions at microscale

The accuracy of the response approximation using the VME method is significantly affected by the conditions imposed along the enrichment domain boundaries. In variational multiscale literature, the typical choice has been the homogeneous Dirichlet boundary condition [5, 27, 6, 15]:

$$\mathbf{u}_\alpha^m(\mathbf{x}, t) = 0; \quad \mathbf{x} \in \Gamma_\alpha \quad (23)$$

The resulting microscale displacement is homogeneous along enrichment domain boundaries and nonzero in the interior, leading to the bubble shape and sometimes referred as residual free bubbles. This boundary condition typically leads to overly stiff response. In order to relax the overconstraint imposed by the homogeneous Dirichlet boundary condition, mixed boundary conditions that has been proposed for elasticity problems in Ref. [31] are generalized for inelastic problems and implemented herein. When the mixed boundary conditions are employed, the resulting microscale displacement is zero at enrichment domain corners and nonzero elsewhere, leading to a canopy shape and referred as the canopy functions. In this approach the boundary tractions along the enrichment domain boundaries are expressed as:

$$\mathbf{t}^r(\mathbf{x}, t) = \hat{\mathbf{t}}_\alpha(\mathbf{x}, t) - \kappa [\mathbf{u}_\alpha^m(\mathbf{x}, t) - \hat{\mathbf{u}}_\alpha(\mathbf{x}, t)] \quad \text{on } \mathbf{x} \in \Gamma_\alpha \equiv \partial\Omega_\alpha; \quad \alpha = 1, 2, \dots, n_{\text{en}}. \quad (24)$$

where $\hat{\mathbf{t}}_\alpha(\mathbf{x}, t)$ and $\hat{\mathbf{u}}_\alpha(\mathbf{x}, t)$ are prescribed traction and displacement along the microscale boundary. Equation (24) constitutes a one-parameter family of boundary conditions that range from a pure Neumann condition when $\kappa = 0$ to a pure Dirichlet condition when $\kappa \rightarrow \infty$ (denoted as $\kappa = \kappa_\infty$). The boundary parameter, κ (such that $0 \leq \kappa < \infty$) therefore controls the boundary constraint stiffness and is adjusted to improve solution accuracy. On the inter-enrichment domain boundaries, $\Gamma_{\alpha\beta}$, the boundary data vanishes (i.e., $\hat{\mathbf{t}}_\alpha(\mathbf{x}, t) = 0$ and $\hat{\mathbf{u}}_\alpha(\mathbf{x}, t) = 0$) and Eq. (24) leads to mixed boundary conditions that range from traction-free to homogeneous Dirichlet conditions. The residual free bubbles are achieved by setting $\kappa = \infty$ on Γ_α .

The proposed mixed boundary condition also improves the approximation of the prescribed conditions along the external boundaries of the problem domain, Ω . Consider the prescribed

traction $\tilde{\mathbf{t}}$ along the external boundary Γ_α^t is variable at the scale of the microstructure. The residual external traction not resolved by the coarse grid is expressed as:

$$\hat{\mathbf{t}}_\alpha(\mathbf{x}, t) = \tilde{\mathbf{t}}_\alpha(\mathbf{x}, t) \equiv \tilde{\mathbf{t}}(\mathbf{x}, t) - \tilde{\mathbf{t}}^M(\mathbf{x}, t) \quad \text{on } \mathbf{x} \in \Gamma_\alpha^t \quad (25)$$

The residual traction is enforced by setting, $\kappa = 0$ at Γ_α^t . Similarly, the residual applied displacement along the boundary Γ_α^u is:

$$\hat{\mathbf{u}}_\alpha(\mathbf{x}, t) = \tilde{\mathbf{u}}_\alpha(\mathbf{x}, t) \equiv \tilde{\mathbf{u}}(\mathbf{x}, t) - \tilde{\mathbf{u}}^M(\mathbf{x}, t) \quad \text{on } \mathbf{x} \in \Gamma_\alpha^u \quad (26)$$

in which, $\tilde{\mathbf{u}}^M(\mathbf{x}, t)$ is the coarse grid approximation of the prescribed displacement. The residual prescribed displacement field is imposed by setting $\kappa = \kappa_\infty$ on Γ_α^u .

In order to satisfy the continuity of the displacement fields across the inter-enrichment domain boundaries, a master-slave coupling approach is employed [31]. Let the neighbor index set for the enrichment domain α be split into master and slave index sets:

$$\begin{aligned} I_\alpha^m &\equiv \{\beta \mid \alpha < \beta \leq n_{\text{en}} \mid \Gamma_{\alpha\beta} \neq \emptyset\}; \\ I_\alpha^s &\equiv \{\beta \mid \beta < \alpha \leq n_{\text{en}} \mid \Gamma_{\alpha\beta} \neq \emptyset\}. \end{aligned} \quad (27)$$

For an arbitrary enrichment domain, α , the displacement continuity is enforced by considering:

$$\mathbf{t}^r(\mathbf{x}, t) = -\kappa_\infty [\mathbf{u}_\alpha^m(\mathbf{x}, t) - \mathbf{u}_\beta^m(\mathbf{x}, t)]; \quad \beta \in I_\alpha^s \text{ and } \mathbf{x} \in \Gamma_\alpha^\beta \quad (28)$$

Employing the mixed boundary conditions as well as the displacement continuity conditions along the inter-enrichment boundaries, the microscale problems defined in Eq. (21) is expressed as:

$$\begin{aligned} \Psi_\alpha^m &\equiv \int_{\Omega_\alpha} \nabla \mathbf{w}_\alpha^m : \boldsymbol{\sigma}(\mathbf{u}^M, \mathbf{u}_\alpha^m) d\Omega - \int_{\Gamma_\alpha^t} \mathbf{w}_\alpha^m \cdot \tilde{\mathbf{t}}_\alpha d\Gamma - \int_{\Gamma_\alpha} \mathbf{w}_\alpha^m \cdot \mathbf{t}^M d\Gamma + \kappa_\infty \int_{\Gamma_\alpha^s} \mathbf{w}_\alpha^m \cdot \mathbf{u}_\alpha^m d\Gamma \\ &+ \kappa \sum_{\beta \in I_\alpha^m} \int_{\Gamma_\alpha^\beta} \mathbf{w}_\alpha^m \cdot \mathbf{u}_\alpha^m d\Gamma + \kappa_\infty \sum_{\beta \in I_\alpha^s} \int_{\Gamma_\alpha^\beta} \mathbf{w}_\alpha^m \cdot (\mathbf{u}_\alpha^m - \mathbf{u}_\beta^m) d\Gamma - \kappa_\infty \int_{\Gamma_\alpha^u} \mathbf{w}_\alpha^m \cdot \tilde{\mathbf{u}} d\Gamma = 0 \end{aligned} \quad (29)$$

The displacement continuity is satisfied by setting $\kappa = \kappa_\infty$ along the interface between the enrichment domain and the substrate domain.

Considering the mixed boundary conditions, the macroscale problem in Eq. (20) becomes:

$$\Psi^M \equiv \int_{\Omega} \nabla \mathbf{w}^M : \boldsymbol{\sigma}(\mathbf{u}^M, \mathbf{u}_\alpha^m) d\Omega - \int_{\Gamma^t} \mathbf{w}^M \cdot \tilde{\mathbf{t}}^M d\Gamma + \kappa_\infty \sum_{\alpha=1}^{n_{\text{en}}} \int_{\Gamma_\alpha^s} \mathbf{w}^M \cdot \mathbf{u}_\alpha^m d\Gamma = 0 \quad (30)$$

In the numerical verification studies below, a sufficiently large but finite value is employed for

κ_∞ for stability and accuracy.

Equations (29) and (30), along with the constitutive equations, constitute the coupled multiscale system. The microscale problem defined over the enrichment domain (Eq. (29)) is coupled to the macroscale response field through the constitutive relationship (i.e., through the first term on the left hand side of Eq. (29)) as well as the macroscale tractions. The macroscale problem is similarly coupled to the microscale response field through the constitutive relationship and the boundary interactions.

4 Computational Implementation

The weak form macroscale equation defined over the problem domain, Ω and the microscale equations defined over each enrichment domain, Ω_α are nonlinear through the constitutive relationship and coupled. The computational implementation of the evolution of this nonlinear coupled system is performed by consistent linearization and finite element discretization, which leads to a coupled algorithmic system. The evaluation of the coupled algorithmic system is performed by employing a sequential coupling algorithm described in Section 4.3.

4.1 Consistent linearization

The macro- and microscale equations along with the constitutive equations are discretized in time to obtain a linearized system of equations evaluated incrementally. The linearization consists of time discretization of the weak forms, stress-strain, kinematic equations and condensation of the constitutive equations to arrive at a system, in which the unknowns are the macro- and microscale displacement fields only. Substituting Eq. (15) into Eq.(4), the stress-strain equation is expressed as a function of the macro- and microscale displacement fields as:

$$\dot{\boldsymbol{\sigma}} = \mathbf{L} : \left[\dot{\boldsymbol{\epsilon}}^M(\mathbf{u}^M) + \sum_{\alpha=1}^{n_{en}} \mathcal{H}(\Omega_\alpha) \dot{\boldsymbol{\epsilon}}_\alpha^m(\mathbf{u}_\alpha^m) - \boldsymbol{\epsilon}^{vp}(\boldsymbol{\sigma}, \mathbf{u}^M, \mathbf{u}^m) \right] \quad (31)$$

in which, $\mathbf{u}^m := \{\mathbf{u}_\alpha^m\}_{\alpha=1}^{n_{en}}$ is the set of all microscale displacement fields. We proceed with the time discretization of the governing equations. Consider a discrete set of instances with the observation period: $\{0, {}_1t, {}_2t, \dots, {}_nt, {}_{n+1}t, \dots, {}_ot\}$. The viscoplastic slip evolution is discretized based on a one-parameter family (referred to as θ -rule):

$$\boldsymbol{\epsilon}^{vp}(\mathbf{x}, t) = (1 - \theta)\boldsymbol{\epsilon}^{vp}(\mathbf{x}, {}_nt) + \theta\boldsymbol{\epsilon}^{vp}(\mathbf{x}, {}_{n+1}t); \quad t \in [{}_nt, {}_{n+1}t] \quad (32)$$

which leads to the following expression for viscoplastic update:

$$\mathbf{P} \equiv {}_{n+1}\boldsymbol{\epsilon}^{vp} - {}_n\boldsymbol{\epsilon}^{vp} - \Delta t (1 - \theta) {}_n\dot{\boldsymbol{\epsilon}}^{vp} - \Delta t \theta {}_{n+1}\dot{\boldsymbol{\epsilon}}^{vp} = 0 \quad (33)$$

in which left subscript n and $n + 1$ indicate the value of a field variable at $n t$ and $n_{+1} t$, respectively (e.g. $n \boldsymbol{\varepsilon}^{vp} = \boldsymbol{\varepsilon}^{vp}(n t)$). The time discretization of Eq. (31) yields:

$$\begin{aligned} \mathbf{R}(\boldsymbol{\sigma}, \mathbf{u}^M, \mathbf{u}^m) \equiv & n_{+1} \boldsymbol{\sigma} - n \boldsymbol{\sigma} - \mathbf{L} : \Delta \boldsymbol{\varepsilon}^M - \sum_{\alpha=1}^{n_{\text{en}}} \mathcal{H}(\Omega_{\alpha}) \mathbf{L} : \Delta \boldsymbol{\varepsilon}_{\alpha}^m + \\ & (1 - \theta) \Delta t \mathbf{L} : n \dot{\boldsymbol{\varepsilon}}^{vp} + \theta \Delta t \mathbf{L} : n_{+1} \dot{\boldsymbol{\varepsilon}}^{vp} = 0 \end{aligned} \quad (34)$$

where $\Delta \boldsymbol{\varepsilon}^M = n_{+1}(\nabla \mathbf{u}^M) - n(\nabla \mathbf{u}^M)$ and $\Delta \boldsymbol{\varepsilon}_{\alpha}^m = n_{+1}(\nabla \mathbf{u}_{\alpha}^m) - n(\nabla \mathbf{u}_{\alpha}^m)$. The system of equations defined by \mathbf{P} , \mathbf{R} along with $\boldsymbol{\Psi}^M$ and $\boldsymbol{\Psi}_{\alpha}^m$ are evaluated using the Newton-Raphson iterative scheme. In what follows, we seek to evaluate the nonlinear multiscale system between $[n t, n_{+1} t]$ from the “known” equilibrium configuration $n t$ to the current configuration at $n_{+1} t$. In what follows, the subscript $n + 1$ from the fields at current configuration is omitted for clarity of presentation. Considering a first order Taylor series approximation of Eq. (34) and forming a Newton iteration yield the following residual for the stress-strain equation:

$$\begin{aligned} \mathbf{R}^{k+1} \approx & \mathbf{R}^k + (\mathbf{I} + \theta \Delta t \mathbf{L} : \mathbf{C}^k) : \delta \boldsymbol{\sigma} - \mathbf{L} : \nabla(\delta \mathbf{u}^M) \\ & - \sum_{\alpha=1}^{n_{\text{en}}} \mathcal{H}(\Omega_{\alpha}) \mathbf{L} : \nabla(\delta \mathbf{u}_{\alpha}^m) + \theta \Delta t \mathbf{L} : \mathbf{G}^k : \delta \boldsymbol{\varepsilon}^{vp} = 0 \end{aligned} \quad (35)$$

in which, superscript k denotes Newton iteration counter; $\delta(\cdot)$ indicates the increment of response field (\cdot) during the current iteration (e.g., $\delta \mathbf{u}^M = \mathbf{u}^{M,k+1} - \mathbf{u}^{M,k}$); \mathbf{I} the fourth order identity tensor; and:

$$\mathbf{C}^k = \left(\frac{\partial \dot{\boldsymbol{\varepsilon}}^{vp}}{\partial \boldsymbol{\sigma}} \right)^k ; \quad \mathbf{G}^k = \left(\frac{\partial \dot{\boldsymbol{\varepsilon}}^{vp}}{\partial \boldsymbol{\varepsilon}^{vp}} \right)^k \quad (36)$$

The expression for derivatives \mathbf{C}^k and \mathbf{G}^k are provided in Appendix A. The linearization of the kinematic equation residual expression (Eq. (33)) yields the following expression:

$$\mathbf{P}^{k+1} \approx \mathbf{P}^k + (\mathbf{I} - \theta \Delta t \mathbf{G}^k) : \delta \boldsymbol{\varepsilon}^{vp} - \theta \Delta t \mathbf{C}^k : \delta \boldsymbol{\sigma} = 0 \quad (37)$$

Rearranging Eq. (37), the viscoplastic strain increment at the current Newton iteration is expressed in terms of the stress increment as:

$$\delta \boldsymbol{\varepsilon}^{vp} = (\mathbf{I} - \theta \Delta t \mathbf{G}^k)^{-1} : (\theta \Delta t \mathbf{C}^k) : \delta \boldsymbol{\sigma} - (\mathbf{I} - \theta \Delta t \mathbf{G}^k)^{-1} : \mathbf{P}^k \quad (38)$$

Substituting Eq. (38) into Eq. (35) condenses out the viscoplastic strain and yields:

$$\mathbf{R}^k - \mathbf{Z}^k + (\mathbf{I} + \theta \Delta t \mathbf{L} : \mathbf{C}^k + \mathbf{H}^k) : \delta \boldsymbol{\sigma} - \mathbf{L} : \nabla(\delta \mathbf{u}^M) - \sum_{\alpha=1}^{n_{\text{en}}} \mathcal{H}(\Omega_{\alpha}) \mathbf{L} : \nabla(\delta \mathbf{u}_{\alpha}^m) = 0 \quad (39)$$

where,

$$\mathbf{H}^k = (\theta \Delta t)^2 \mathbf{L} : \mathbf{G}^k : (\mathbf{I} - \theta \Delta t \mathbf{G}^k)^{-1} : \mathbf{C}^k \quad (40a)$$

$$\mathbf{Z}^k = \theta \Delta t \mathbf{L} : \mathbf{G}^k : (\mathbf{I} - \theta \Delta t \mathbf{G}^k)^{-1} : \mathbf{P}^k \quad (40b)$$

Equation (39) can be solved with respect to the stress increment, resulting in

$$\delta \boldsymbol{\sigma}(\delta \mathbf{u}^M, \delta \mathbf{u}_\alpha^m) = \hat{\mathbf{L}}^k : \nabla(\delta \mathbf{u}^M) + \sum_{\alpha=1}^{n_{\text{en}}} \mathcal{H}(\Omega_\alpha) \hat{\mathbf{L}}^k : \nabla(\delta \mathbf{u}_\alpha^m) - \mathbf{Q}^k : (\mathbf{R}^k - \mathbf{Z}^k) \quad (41)$$

where

$$\hat{\mathbf{L}}^k = (\mathbf{L}^{-1} + \theta \Delta t \mathbf{C}^k + \mathbf{L}^{-1} : \mathbf{H}^k)^{-1} \quad (42)$$

$$\mathbf{Q}^k = (\mathbf{I} + \theta \Delta t \mathbf{L} : \mathbf{C}^k + \mathbf{H}^k)^{-1} \quad (43)$$

The linearized weak form equilibrium equation for the macroscale is expressed in terms of the stress and the microscale displacement increments as:

$$\Psi^{M,k+1} \approx \Psi^{M,k} + \int_{\Omega} \nabla \mathbf{w}^M : \delta \boldsymbol{\sigma} \, d\Omega + \sum_{\alpha=1}^{n_{\text{en}}} \kappa_\infty \int_{\Gamma_\alpha^s} \mathbf{w}^M \cdot \delta \mathbf{u}_\alpha^m \, d\Gamma = 0 \quad (44)$$

Similarly, the linearization of the microscale problem over Ω_α ($\alpha = 1, 2, \dots, n_{\text{en}}$):

$$\begin{aligned} \Psi_\alpha^{m,k+1} \approx & \Psi_\alpha^{m,k} + \int_{\Omega_\alpha} \nabla \mathbf{w}_\alpha^m : \delta \boldsymbol{\sigma} \, d\Omega - \int_{\Gamma_\alpha} \mathbf{w}_\alpha^m \cdot \delta \mathbf{t}^M \, d\Gamma + \kappa_\infty \int_{\Gamma_\alpha^s} \mathbf{w}_\alpha^m \cdot \delta \mathbf{u}_\alpha^m \, d\Gamma \\ & + \sum_{\beta \in I_\alpha^m} \kappa \int_{\Gamma_\alpha^\beta} \mathbf{w}_\alpha^m \cdot \delta \mathbf{u}_\alpha^m \, d\Gamma + \sum_{\beta \in I_\alpha^s} \kappa_\infty \int_{\Gamma_\alpha^\beta} \mathbf{w}_\alpha^m \cdot (\delta \mathbf{u}_\alpha^m - \delta \mathbf{u}_\beta^m) \, d\Gamma = 0 \end{aligned} \quad (45)$$

where $\delta \mathbf{t}^M = \boldsymbol{\sigma}^{k+1}(\mathbf{u}^{M,k+1}, \mathbf{0}) - \boldsymbol{\sigma}^k(\mathbf{u}^{M,k}, \mathbf{0})$ is the macroscale traction over the microscale domain boundaries computed from Eq. (41). Substituting Eq. (41) into Eqs. (44) and (45), the linearized governing equations for the macroscale problems is expressed as:

$$\begin{aligned} \int_{\Omega} \nabla \mathbf{w}^M : \hat{\mathbf{L}}^k : \nabla(\delta \mathbf{u}^M) \, d\Omega = & - \sum_{\alpha=1}^{n_{\text{en}}} \int_{\Omega_\alpha} \nabla \mathbf{w}^M : \hat{\mathbf{L}}^k : \nabla(\delta \mathbf{u}_\alpha^m) \, d\Omega \\ & + \int_{\Omega} \nabla \mathbf{w}^M : \mathbf{Q}^k : (\mathbf{R}^k - \mathbf{Z}^k) \, d\Omega - \sum_{\alpha=1}^{n_{\text{en}}} \kappa_\infty \int_{\Gamma_\alpha^s} \mathbf{w}^M \cdot \delta \mathbf{u}_\alpha^m \, d\Gamma - \Psi^{M,k} \end{aligned} \quad (46)$$

and for the microscale domains over Ω_α ($\alpha = 1, 2, \dots, n_{\text{en}}$):

$$\begin{aligned}
\int_{\Omega_\alpha} \nabla \mathbf{w}_\alpha^m : \hat{\mathbf{L}}^k : \nabla(\delta \mathbf{u}_\alpha^m) d\Omega &= - \int_{\Omega_\alpha} \nabla \mathbf{w}_\alpha^m : \hat{\mathbf{L}}^k : \nabla(\delta \mathbf{u}^M) d\Omega + \int_{\Omega_\alpha} \nabla \mathbf{w}_\alpha^m : \mathbf{Q}^k : (\mathbf{R}^k - \mathbf{Z}^k) d\Omega \\
&+ \int_{\Gamma_\alpha} \mathbf{w}_\alpha^m \cdot \left[\hat{\mathbf{L}}^k : \nabla(\delta \mathbf{u}^M) - \mathbf{Q}^k : (\mathbf{R}^k - \mathbf{Z}^k) \right] d\Gamma - \kappa_\infty \int_{\Gamma_\alpha^s} \mathbf{w}_\alpha^m \cdot \delta \mathbf{u}_\alpha^m d\Gamma \\
&- \sum_{\beta \in I_\alpha^m} \kappa \int_{\Gamma_\alpha^\beta} \mathbf{w}_\alpha^m \cdot \delta \mathbf{u}_\alpha^m d\Gamma - \sum_{\beta \in I_\alpha^s} \kappa_\infty \int_{\Gamma_\alpha^\beta} \mathbf{w}_\alpha^m \cdot (\delta \mathbf{u}_\alpha^m - \delta \mathbf{u}_\beta^m) d\Gamma - \Psi_\alpha^{m,k}
\end{aligned} \tag{47}$$

It can be observed from Eqs. (46) and (47) the value of the boundary parameter κ for all inter-enrichment domain boundaries is set as a fixed value for all inter-enrichment domains and throughout the loading process. The value of the boundary parameter for the parts of the enrichment domain boundaries that overlap with prescribed Dirichlet boundaries and enrichment domain-substrate domain interface is set to a very large value (κ_∞). The κ parameter is set to zero when the enrichment domain boundary lies along prescribed Neumann boundaries, as described in Section 3.1.

4.2 Finite element discretization

Equations (46) and (47) are evaluated using the finite element method. Consider the following finite element spaces for the macro- and microscale response fields:

$$\mathcal{V}^M(\Omega) \equiv \left\{ \mathbf{u}^M(\mathbf{x}, t) \mid \mathbf{u}^M(\mathbf{x}, t) = \sum_{A=1}^{N_D} N_A(\mathbf{x}) \hat{\mathbf{u}}_A^M(t); \hat{\mathbf{u}}_A^M(t) = \hat{\mathbf{u}}^M(\mathbf{x}_A, t) \text{ if } \mathbf{x}_A \in \Gamma^u \right\} \tag{48}$$

$$\mathcal{V}_\alpha^m(\Omega_\alpha) \equiv \left\{ \mathbf{u}_\alpha^m(\mathbf{x}, t) \mid \mathbf{u}_\alpha^m(\mathbf{x}, t) = \sum_{a=1}^{n_{d_\alpha}} n_{\alpha,a}(\mathbf{x}) \hat{\mathbf{u}}_{\alpha,a}^m(t); \hat{\mathbf{u}}_{\alpha,a}^m(t) = \hat{\mathbf{u}}_\alpha(\mathbf{x}_\alpha, t) \text{ if } \mathbf{x}_\alpha \in \Gamma_\alpha^u \right\} \tag{49}$$

in which, N_D and n_{d_α} denote the number of nodes in the macroscale discretization Ω , and the microscale discretization of Ω_α , respectively; N_A and $n_{\alpha,a}$ are the shape functions for the macroscale and microscale fields, respectively; \mathbf{x}_A and \mathbf{x}_α are the corresponding nodal coordinates. Overhat denotes the nodal coordinates of the corresponding response field. The present formulation considers the macroscale and microscale grids to be nested, which means each enriched macroscale finite element coincides with a corresponding enrichment domain in the enrichment region. It is also possible to consider enrichment domains to be independent of the macroscale mesh, i.e., each enrichment domain may occupy multiple macroscale elements. While the general formulation is unaffected by this generalization, the implementation could be quite different and not considered in this study. Employing the standard Bubnov-Galerkin approach, the test functions are taken to be discretized using the same macro- and microscale shape functions.

Substitute Eqs. (48) and (49) into the macroscale weak form (Eq. (46)) yields the discrete macroscale system. At the $(k + 1)$ th iteration of the current time step, $n_{+1}t$, the macroscale weak form takes the form expressed as:

$$\mathbf{K} \delta \hat{\mathbf{u}}^M = \delta \mathbf{f} \quad (50)$$

where,

$$\delta \hat{\mathbf{u}}^M = \left\{ \left(\delta \hat{\mathbf{u}}_1^{M,k+1} \right)^T, \left(\delta \hat{\mathbf{u}}_2^{M,k+1} \right)^T, \dots, \left(\delta \hat{\mathbf{u}}_{N_D}^{M,k+1} \right)^T \right\}^T \quad (51)$$

in which, $\delta \hat{\mathbf{u}}_A^{M,k+1} = \hat{\mathbf{u}}_A^{M,k+1} - \hat{\mathbf{u}}_A^{M,k}$ ($A = 1, 2, \dots, N_D$) and $\delta \hat{\mathbf{u}}^M$ denotes the increment of the macroscale nodal displacement coefficients at the $(k + 1)$ th iteration. The tangent stiffness matrix is expressed as:

$$\mathbf{K} = \mathbf{A}_{A,B} \int_{\Omega} \nabla N_A \cdot \hat{\mathbf{L}}^k \cdot \nabla N_B \, d\Omega \quad (52)$$

in which \mathbf{A} denotes the standard finite element assembly operator. Within the macroscale elements associated with an enrichment domain, the tensor of tangent moduli, $\hat{\mathbf{L}}$ oscillates due to the heterogeneity of the microstructure. The integral is resolved and evaluated based on the underlying coarse grid on enriched elements. The force increment in the current iteration, $\delta \mathbf{f}$ is expressed as:

$$\begin{aligned} \delta \mathbf{f} = \mathbf{A}_A \left\{ - \sum_{\alpha=1}^{n_{\text{en}}} \sum_{a=1}^{n_{d_\alpha}} \left[\int_{\Omega_\alpha} \nabla N_A \cdot \hat{\mathbf{L}}^k \cdot \nabla n_{\alpha,a} \, d\Omega \, \delta \hat{\mathbf{u}}_{\alpha,a}^m + \kappa_\infty \int_{\Gamma_\alpha^s} N_A \, n_{\alpha,a} \, d\Gamma \, \delta \hat{\mathbf{u}}_\alpha^m \right] \right. \\ \left. + \int_{\Omega} \nabla N_A \cdot \mathbf{Q}^k : (\mathbf{R}^k - \mathbf{Z}^k) \, d\Omega \right\} - \Psi^{M,k} \end{aligned} \quad (53)$$

The discrete microscale system for the enriched domain, α , is obtained by substituting Eqs. (48) and (49) into the microscale weak form (Eq. (47)):

$$\mathbf{K}_\alpha \delta \hat{\mathbf{u}}_\alpha^m = \delta \mathbf{f}_\alpha \quad (54)$$

where,

$$\delta \hat{\mathbf{u}}_\alpha^m = \left\{ \left(\delta \hat{\mathbf{u}}_{\alpha,1}^{m,k+1} \right)^T, \left(\delta \hat{\mathbf{u}}_{\alpha,2}^{m,k+1} \right)^T, \dots, \left(\delta \hat{\mathbf{u}}_{\alpha,n_{d_\alpha}}^{m,k+1} \right)^T \right\}^T \quad (55)$$

in which, $\delta \hat{\mathbf{u}}_{\alpha,a}^{m,k+1} = \hat{\mathbf{u}}_{\alpha,a}^{m,k+1} - \hat{\mathbf{u}}_{\alpha,a}^{m,k}$ ($a = 1, 2, \dots, n_{d_\alpha}$) and $\delta \hat{\mathbf{u}}_\alpha^m$ denotes the increment of the microscale nodal displacement coefficients at the $(k + 1)$ th iteration. The microscale tangent

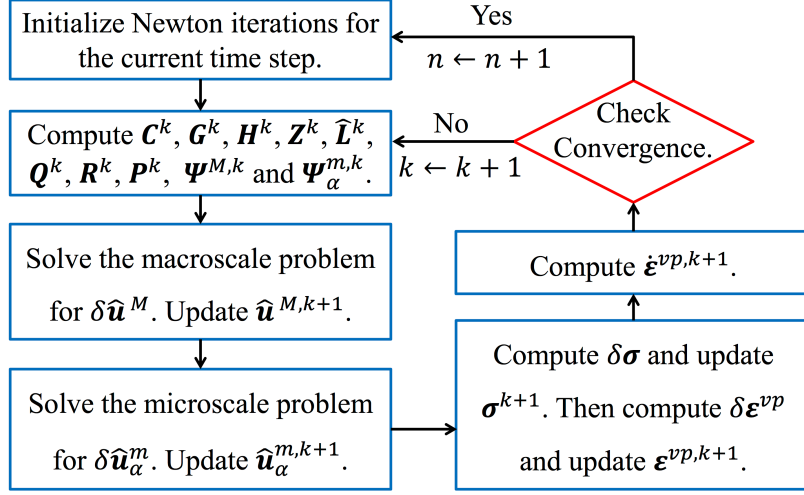


Figure 2: Solution algorithm

stiffness matrix is assembled as:

$$\mathbf{K}_\alpha = \mathbf{A}_{a,b} \left\{ \int_{\Omega_\alpha} \nabla n_{\alpha,a} \cdot \hat{\mathbf{L}}^k \cdot \nabla n_{\alpha,b} d\Omega_\alpha + \kappa_\infty \int_{\Gamma_\alpha^s} n_{\alpha,a} n_{\alpha,b} d\Gamma + \kappa \int_{\Gamma_\alpha^{\beta m}} n_{\alpha,a} n_{\alpha,b} d\Gamma + \kappa_\infty \int_{\Gamma_\alpha^{\beta s}} n_{\alpha,a} n_{\alpha,b} d\Gamma \right\} \quad (56)$$

and the corresponding force increment is expressed as:

$$\delta \mathbf{f}_\alpha = \mathbf{A}_a \left\{ - \int_{\Omega_\alpha} \nabla n_{\alpha,a} \cdot \hat{\mathbf{L}}^k \cdot \nabla N_B d\Omega \delta \hat{\mathbf{u}}_B^M(t) + \int_{\Omega_\alpha} \nabla n_{\alpha,a} \cdot \mathbf{Q}^k : (\mathbf{R}^k - \mathbf{Z}^k) d\Omega + \int_{\Gamma_\alpha} n_{\alpha,a} \left[\hat{\mathbf{L}}^k : \nabla(\delta \mathbf{u}^M) - \mathbf{Q}^k : (\mathbf{R}^k - \mathbf{Z}^k) \right] d\Gamma + \kappa_\infty \int_{\Gamma_\alpha^{\beta s}} n_{\alpha,a} \delta \mathbf{u}_\beta^m d\Gamma \right\} - \Psi_\alpha^{m,k} \quad (57)$$

where, $\Gamma_\alpha^{\beta m} \equiv \{\Gamma_\alpha^\beta | \beta \in I_\alpha^m\}$, $\Gamma_\alpha^{\beta s} \equiv \{\Gamma_\alpha^\beta | \beta \in I_\alpha^s\}$ and subscript B indicates the corresponding coarse scale element. Equations (50) and (54) constitute the linearized system of equations that are evaluated for the macro- and microscale problems. Each microscale problem defined over an enrichment domain is coupled to the macroscale problem as well as the enrichment domain problems that share a common boundary and has a master surface (i.e., all enrichment domain problems in I_α^s). The coupling is through the force vector (i.e., $\delta \mathbf{f}_\alpha(\hat{\mathbf{u}}^M, \{\delta \mathbf{u}_\beta^m | \beta \in I_\alpha^s\})$). The macroscale problem is coupled to the enrichment domain problems (i.e., $\delta \mathbf{f}(\{\hat{\mathbf{u}}_\alpha^m\}_{\alpha=1}^{n_{\text{en}}})$). This coupled system of equations is evaluated using a staggered solution algorithm defined below.

4.3 Computational algorithm

The VME formulation for the elasto-viscoplastic problem is implemented using the C++ computer language with the commercial software package, Diffpack [22]. Diffpack is an object-oriented development framework for the numerical solution of partial differential equations. It provides a library of C++ classes to facilitate development of solution algorithms for complex PDEs [22]. The overall solution strategy is to evaluate the coupled system of multiscale equations summarized in Fig. 2. At an arbitrary time $n t$, the system is in equilibrium with the constitutive relations satisfied at macro- and microscale. The algorithm seeks to find the equilibrium state at $n_{+1} t$ as follows:

Given: ${}_n \hat{\mathbf{u}}^M, {}_n \hat{\mathbf{u}}_\alpha^m, {}_n \boldsymbol{\varepsilon}^{vp}, {}_n \dot{\boldsymbol{\varepsilon}}^{vp}, {}_n \boldsymbol{\sigma}$ at time $n t$.

Find: $\hat{\mathbf{u}}^M, \hat{\mathbf{u}}_\alpha^m, \boldsymbol{\varepsilon}^{vp}, \dot{\boldsymbol{\varepsilon}}^{vp}, \boldsymbol{\sigma}$ at time $n_{+1} t$.

1. Initialize Newton iterations by setting: $k=0$, $\hat{\mathbf{u}}^{M,0} = {}_n \hat{\mathbf{u}}^M$, $\hat{\mathbf{u}}_\alpha^{m,0} = {}_n \hat{\mathbf{u}}_\alpha^m$, $\boldsymbol{\varepsilon}^{vp,0} = {}_n \boldsymbol{\varepsilon}^{vp}$, $\dot{\boldsymbol{\varepsilon}}^{vp,0} = {}_n \dot{\boldsymbol{\varepsilon}}^{vp}$, $\boldsymbol{\sigma}^0 = {}_n \boldsymbol{\sigma}$, and $\delta \mathbf{u}_\alpha^m = 0$, where $1 \leq \alpha \leq n_{\text{en}}$.
2. While not converged:
 - a) Compute $\mathbf{C}^k, \mathbf{G}^k, \mathbf{H}^k, \mathbf{Z}^k, \hat{\mathbf{L}}^k, \mathbf{Q}^k, \mathbf{R}^k, \mathbf{P}^k, \boldsymbol{\Psi}^{M,k}$ and $\boldsymbol{\Psi}_\alpha^{m,k}$ for the multiscale system from Eqs. (36), (40a), (40b), (42), (43), (34), (33), (30) and (29), respectively.
 - b) Solve the macroscale problem (Eq. (50)) for $\delta \hat{\mathbf{u}}^M$ over the structural domain, Ω , using the microscale increments $\delta \mathbf{u}_\alpha^m$ from the previous iteration.
 - c) Update the macroscopic displacement coefficients, $\hat{\mathbf{u}}^{M,k+1} = \hat{\mathbf{u}}^{M,k} + \delta \hat{\mathbf{u}}^M$.
 - d) Solve the microscale problem (i.e., Eq. (54)) for $\delta \hat{\mathbf{u}}_\alpha^m$ over each enriched domain, Ω_α ($1 \leq \alpha \leq n_{\text{en}}$).
 - e) Update the microscopic displacement coefficients, $\hat{\mathbf{u}}_\alpha^{m,k+1} = \hat{\mathbf{u}}_\alpha^{m,k} + \delta \hat{\mathbf{u}}_\alpha^m$.
 - f) At every integration point in macro, and micro problems:
 - i) Employing $\delta \hat{\mathbf{u}}^M$ and $\delta \hat{\mathbf{u}}_\alpha^m$, compute current stress increment $\delta \boldsymbol{\sigma}$ using Eq. (41). Update stress $\boldsymbol{\sigma}^{k+1} = \boldsymbol{\sigma}^k + \delta \boldsymbol{\sigma}$.
 - ii) Compute $\delta \boldsymbol{\varepsilon}^{vp}$ using Eq. (38). Update viscoplastic strain $\boldsymbol{\varepsilon}^{vp,k+1} = \boldsymbol{\varepsilon}^{vp,k} + \delta \boldsymbol{\varepsilon}^{vp}$.
 - g) Compute viscoplastic strain rate $\dot{\boldsymbol{\varepsilon}}^{vp,k+1}$ using Eq. (5).
 - h) Check for convergence at macroscale and microscale problems:
$$\begin{cases} e^M &= \|\hat{\mathbf{u}}^{M,k+1} - \hat{\mathbf{u}}^{M,k}\|_2 \leq \text{Convergence tolerance} \\ e_\alpha^m &= \|\hat{\mathbf{u}}_\alpha^{m,k+1} - \hat{\mathbf{u}}_\alpha^{m,k}\|_2 \leq \text{Convergence tolerance} \end{cases} \quad (58)$$
 - i) If convergence criterion are not satisfied, set iteration counter $k \leftarrow k+1$ and proceed with the next iteration.
3. Repeat step 2 with $n \leftarrow n+1$ until the end of the observation period.

Table 1: Materials parameters.

Material type	E [GPa]	ν	A [MPa]	B [MPa]	n	q	γ [MPa-hr] ⁻¹
Substrate	120.8	0.32	500	700	0.93	1.0	1.0
Phase I	110.8	0.32	400	200	0.96	1.0	1.0
Phase II	130.8	0.32	600	1200	0.90	1.0	1.0

The staggered form of the solution algorithm is achieved by solving the macroscale system using the microscale displacement coefficients from the previous iteration (Step 2b)). The staggering order, which is evaluating the macroscale problem prior to the microscale problems, is natural since the loading on the domain is expected to be primarily at the macroscale (i.e., typically but not necessarily $\hat{\mathbf{u}}_\alpha = 0$ on Γ_α^u and $\hat{\mathbf{t}}_\alpha = 0$ on Γ_α^t). The effect of stagger ordering does not have a notable effect on the solution. The convergence of the multiscale system is assessed when both the macroscale system and the enrichment domain problems simultaneously converge. A detailed convergence study on the staggered solution algorithm in the context of elasticity has been provided in Ref. [30] and not included in this manuscript.

5 Numerical Verification

The implementation of the VME method for elasto-viscoplastic problems is verified using numerical simulations. The VME model predictions are compared to the direct numerical simulations using the finite element method. In the direct numerical simulations, the heterogeneities within the problem domain is fully resolved. In all simulations below, the domain is taken to consist of three separate materials. The heterogeneous material microstructure consists of two phases. A third material that approximates the properties of the composite domain is employed to idealize the behavior at the substrate domain. The material properties of the two phases and the substrate are provided in Table 1 and the constitutive relationship of these materials under unidirectional tension is plotted in Fig. 3.

The boundary condition parameter κ is relatively sensitive to the microstructural topology as well as the constituent material parameters. A sensitivity analysis and a parameter selection strategy are outlined in Ref. [31]. In this manuscript, the selection of the boundary parameter is performed by subjecting a representative cell to pure uniaxial and shear loading, and choosing the boundary parameter which minimizes the discrepancy between the direct finite element analysis of the microstructure and the corresponding VME model (described in Section 5.1). The boundary parameter employed in the analysis of the specimen with a center notch (Section 5.2) uses the boundary parameter selected as such.

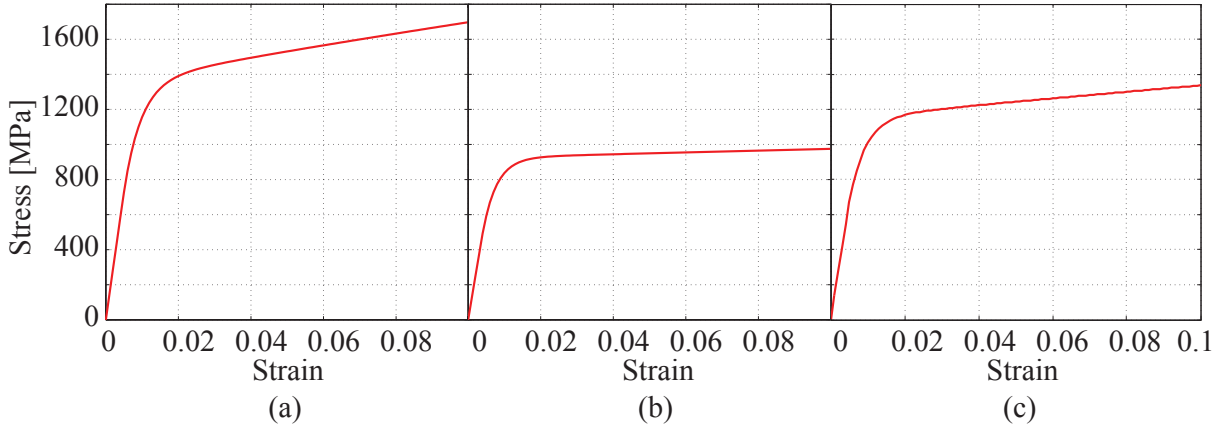


Figure 3: Stress-strain behavior of the constituent materials under uniaxial tension: (a) phase I; (b) phase II; and (c) substrate material.

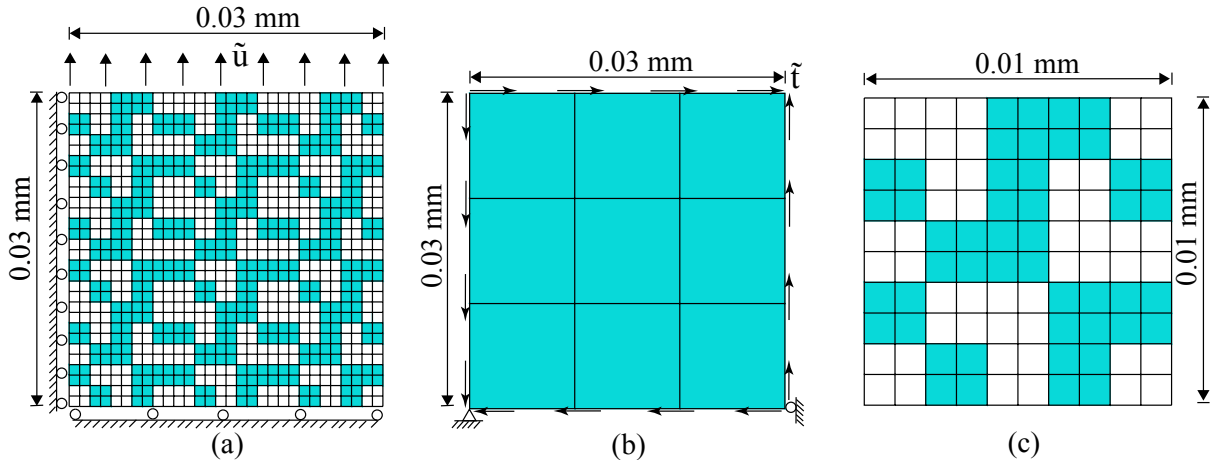


Figure 4: Numerical models of the square specimen: (a) direct finite element discretization and sketch for uniform tensile load; (b) macroscale discretization and sketch for pure shear load; and (c) microscale discretization of an enrichment domain.

5.1 Effect of the boundary parameter

In this section, the effect of the mixed boundary parameter, κ , on the accuracy characteristics of the VME method in the context of elasto-viscoplastic behavior is investigated. The effect of the mixed boundary parameter on composite media with elastic modulus contrast has been previously investigated in Ref. [31]. A 2-D plane strain, composite domain with a two-phase microstructure is considered as shown in Fig 4a. The geometry and the discretization used in the VME simulations are shown in Figs. 4b,c. The heterogeneity in the original problem domain is exactly obtained by the repetition of the microstructure (Fig. 4c) in a 3-by-3 tile. Phase I and phase II materials are identified as dark and light elements, respectively. The behavior of the square composite domain was investigated under displacement controlled uniform tension and shear conditions. The loading was applied at the uniform strain rate of approximately

$3 \times 10^{-4}/s$. All 9 macroscale elements are taken to be enriched in the VME simulations, which means that the enrichment region is the entire problem domain. The macroscale grid ensures that the central enriched domain has all four boundaries of inter-enrichment type. Each of the enrichment domains are discretized fine enough to ensure that further discretization does not noticeably affect the simulation accuracy. The direct finite element discretization and the microscale discretization are taken to have the same element size. The time step size is determined such that further refinement does not change the results significantly. The convergence tolerance employed in the simulations is set to 1×10^{-6} .

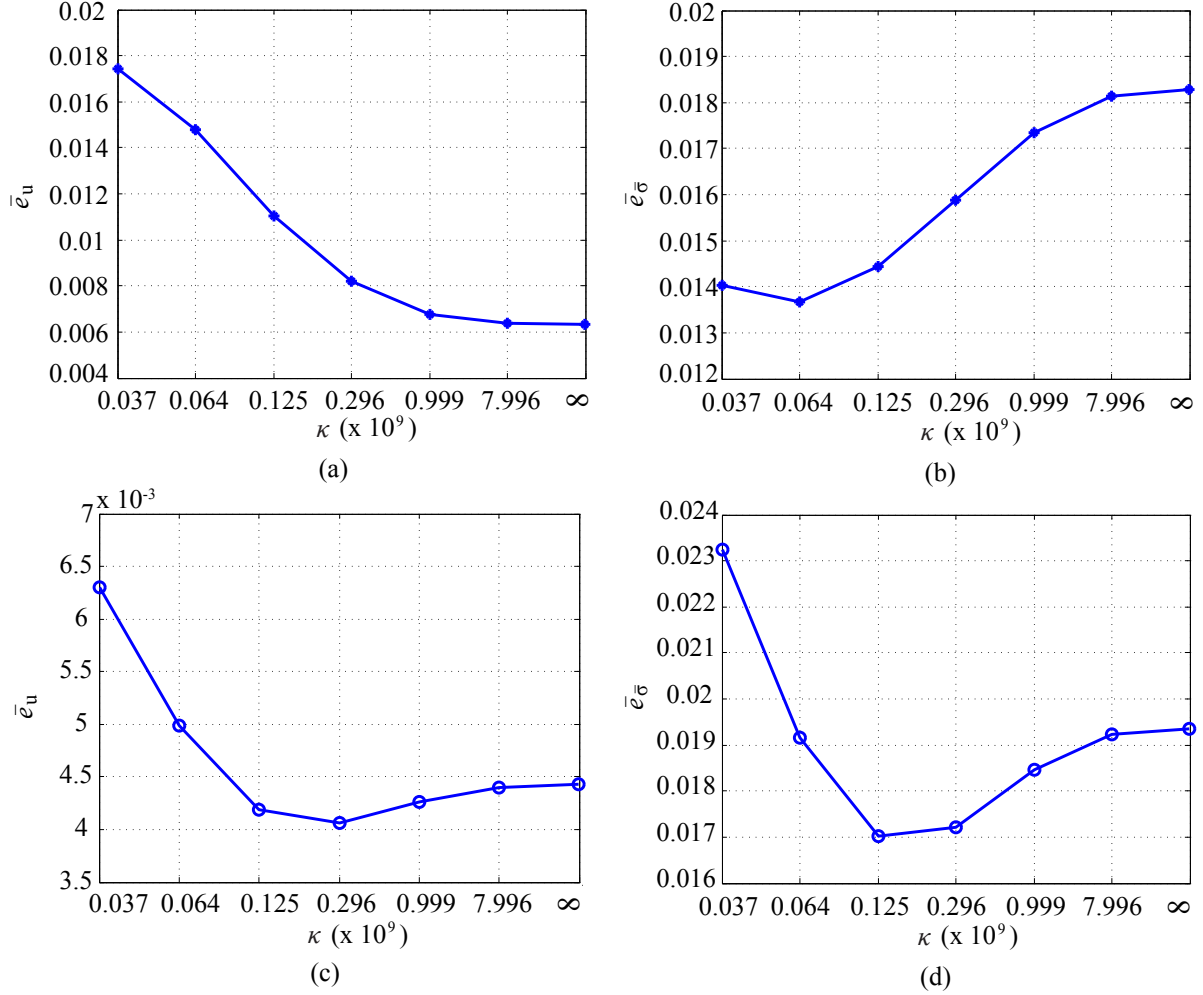


Figure 5: Time averaged error as a function of the boundary parameter: (a) displacement error under tensile loading; (b) equivalent stress error under tensile loading; (c) displacement error under shear loading; and (d) equivalent stress error under shear loading.

Figure 5 illustrates the time averaged errors in displacement and stress under tensile and shear loading conditions. The errors of the proposed multiscale method are compared to the direct finite element analysis as a function of the boundary parameter, κ . The error over the

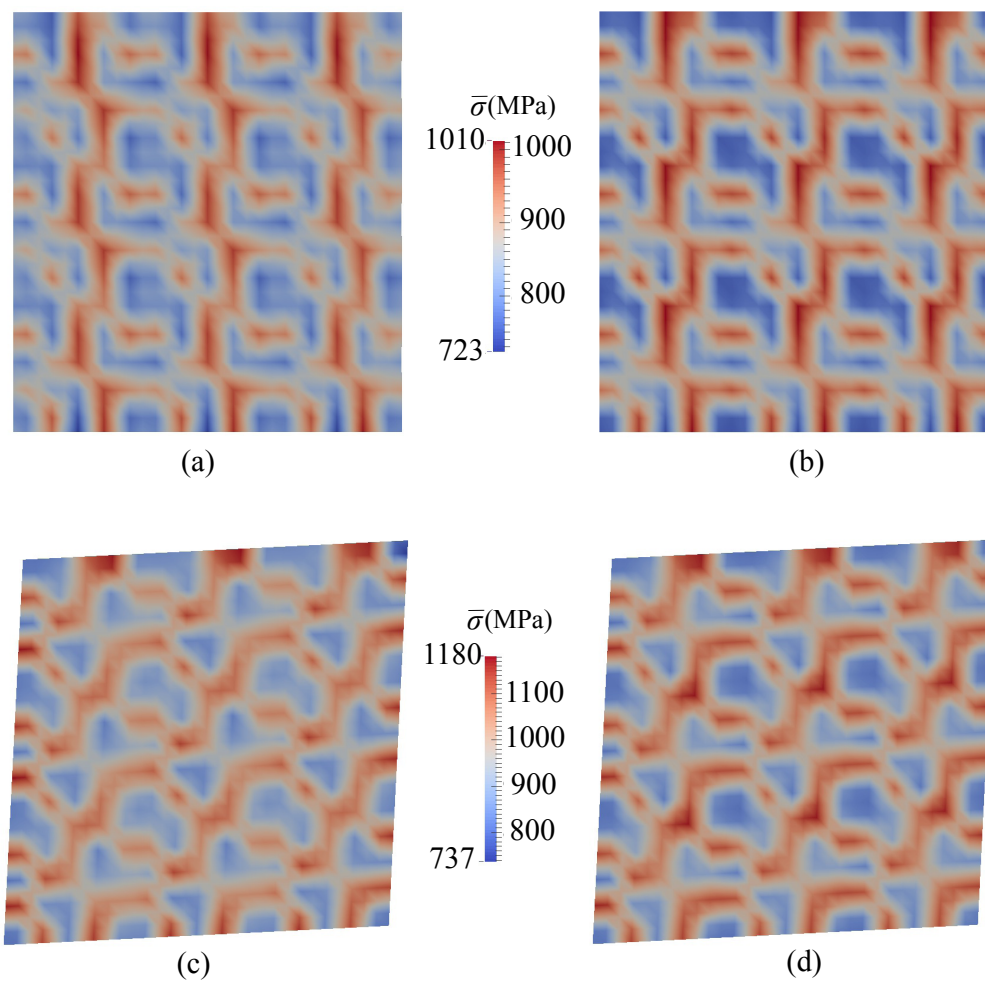


Figure 6: Equivalent stress contours at 3.0×10^{-4} mm applied displacement. (a) Reference model under uniform tension; (b) VME model under uniform tension; (c) reference model under shear; and (d) VME model under shear.

entire boundary domain at an arbitrary time, t , is computed as:

$$e_\phi(t) = \frac{\sum_{\alpha=1}^{n_{\text{en}}} \|\phi^{\text{FEM}}(\mathbf{x}, t) - \phi^{\text{VME}}(\mathbf{x}, t)\|_{2, \Omega_\alpha}}{\sum_{\alpha=1}^{n_{\text{en}}} \|\phi^{\text{FEM}}(\mathbf{x}, t)\|_{2, \Omega_\alpha}} \quad (59)$$

where, ϕ^{FEM} and ϕ^{VME} denotes a response field (i.e., displacement or equivalent stress) computed using the direct finite element method and the VME, respectively, $\|\cdot\|_{2, \Omega_\alpha}$ is the L_2 norm of the displacement field computed over Ω_α . When the numerical specimen is subjected to uniform tension, the displacement error is minimized when homogeneous Dirichlet boundary conditions are employed. In contrast, the time averaged error in the equivalent stress is minimized at a slightly relaxed boundary parameter with $\kappa \in [3.7 \times 10^7, 1.25 \times 10^8]$. Under the shear load, the displacement and equivalent stress errors are minimized at the boundary parameter values of $\kappa = 2.96 \times 10^8$ and $\kappa = 1.25 \times 10^8$, respectively. The results indicate limited improvement of accuracy in the displacement and stress fields when the boundary condition is slightly relaxed from the homogeneous Dirichlet conditions. In the case of uniaxial tension loading, the errors in the stress computations improve by approximately 32% when the optimal boundary parameter is employed. The trends in errors follow a similar trend to those computed in the context of elasticity problems provided in Ref. [31]. Figures 6a,b compare the contours of equivalent stress fields computed by the proposed model and the direct finite element method at time $t = 36$ seconds and under an applied uniform tensile displacement of 3.0×10^{-4} mm. Equivalent contours at $t = 36$ seconds and under an applied shear displacement of 3.0×10^{-4} mm are shown in Figs. 6c,d for the VME and direct FEM methods, respectively. The contours from the VME simulations are reconstructed from the micro- and macroscale solutions at the post-processing stage. In both cases, there is a close agreement in the stress fields computed by the reference and the multiscale simulations.

5.2 Specimen with a center notch

The proposed multiscale method is further verified using the numerical analysis of a specimen with a center notch subjected to uniform tensile loading in the vertical direction. The dimensions of the rectangular specimen and the center notch are $0.8 \text{ mm} \times 0.4 \text{ mm}$ with a $0.4 \text{ mm} \times 0.04 \text{ mm}$, respectively. Due to symmetry, only a quarter of the specimen is modeled. The two-phase microstructure of the domain and the material properties of the phases are taken to be identical to the example provided in Section 5.1. The specimen was subjected to uniform displacement controlled tensile loading in the vertical direction. The maximum amplitude of the loading was 0.01 mm applied at a rate of $5.6 \times 10^{-5} \text{ mm/sec}$.

The geometry, boundary conditions of the problem domain, as well as the macro- and

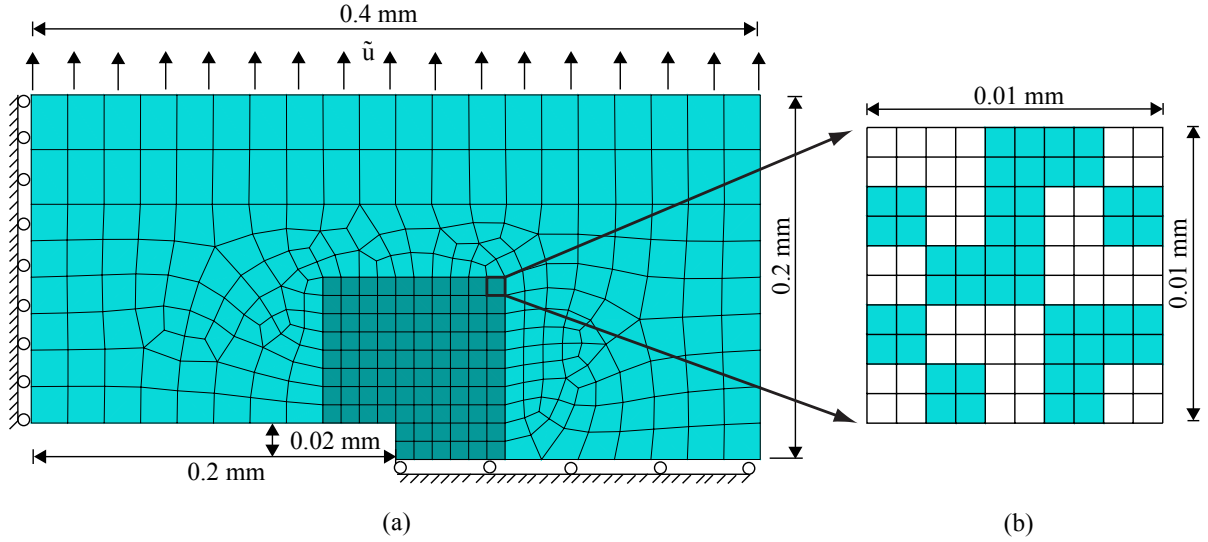


Figure 7: Multiscale variational enrichment model of the specimen with a notch: (a) sketch and discretization of the macroscale discretization; and (b) microscale discretization of an enrichment domain in the enrichment region.

microscale discretization employed in the VME approach is shown in Fig. 7. A $0.1 \text{ mm} \times 0.1 \text{ mm}$ square domain at the center of the specimen is chosen as the enrichment region. The macroscale mesh consists of 314 quadrilateral macroscale elements, 92 of which are enriched. Each enriched element is associated with an identical microscale geometry shown in Fig. 7b. The microscale mesh consists of 100 quadrilateral elements. Outside the enrichment region (i.e., the substrate region), substrate material properties shown in Table 1 are employed. The VME simulations were conducted using homogeneous Dirichlet boundary conditions, as well as using the mixed boundary conditions with $\kappa = 2.96 \times 10^8$. The optimal mixed boundary parameter identified under the shear loading in the previous section is employed since the plastic deformation occurs under shear. The performance of the VME approach was assessed by comparing the model results to the direct numerical simulations, in which the enrichment region is fully resolved. The reference mesh is shown in Fig. 8 and consists of 11276 quadrilateral elements. The size of the elements within the enrichment domain is taken to be the same as the size of the elements in the microscale mesh used in the VME approach. The substrate region is meshed with coarser elements. A transition region is included to ensure mesh conformity.

Figure 9 illustrates the evolution of the errors in the displacement and equivalent stress within the enrichment region as a function of simulation time. The errors are computed using Eq. (59). The figure includes the VME simulations performed using the homogeneous Dirichlet and optimal shear boundary conditions. The errors in the displacement computed using the homogeneous Dirichlet and the optimal shear boundary conditions remained within 3% and

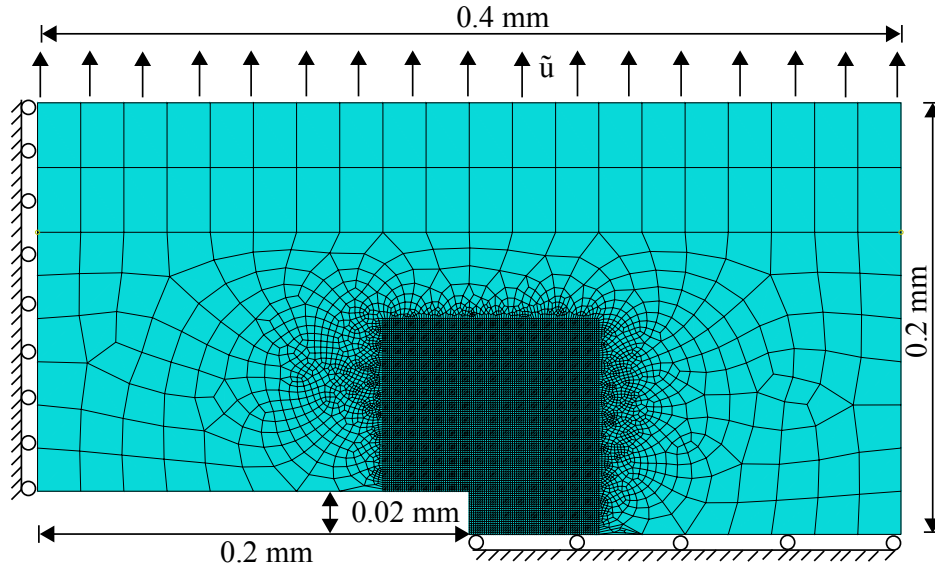


Figure 8: Discretization of the direct finite element model of the notched specimen.

1.5%, respectively. The errors in the stress computed using the two boundary conditions are within 8.5% and 6%, respectively. In the case of the homogeneous Dirichlet boundary conditions, the displacement errors accumulate as a function of increasing plastic strain, whereas the optimal shear boundary condition has less sensitivity to the plastic strain magnitude. The proposed multiscale approach has reasonable accuracy characteristics compared to the reference model for both types of boundary conditions.

Figure 10 shows the comparison of the overall force displacement curves computed using the reference finite element method and the proposed VME method. The VME simulations performed using the two types of boundary conditions resulted in near identical force-displacement curves. Figure 10 clearly shows that the proposed approach is able to accurately capture the overall elasto-viscoplastic response. In addition to the overall behavior, the local deformation and stresses are very accurately captured using the proposed VME approach. The equivalent stress contours obtained based on the reference and the VME method are compared in Fig. 11. The equivalent stress contours correspond to the applied peak load at the end of the simulations. The stress contours for the VME approach is reconstructed using the enrichment domain solutions at the post-processing stage. The local stress distributions show an oscillatory behavior around the notch tip, due to the heterogeneous microstructure. The oscillatory behavior is well captured using the proposed VME approach, pointing to its ability to reproduce the local stress fields within the critical regions of the problem domain.

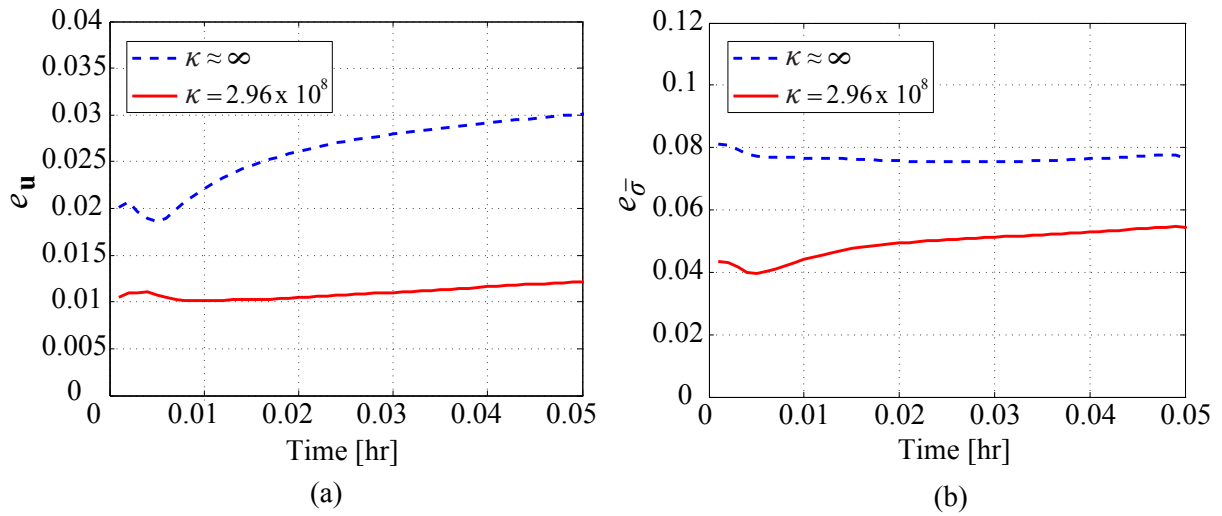


Figure 9: Errors as a function of simulation time: (a) error in displacement; and (b) error in equivalent stress.

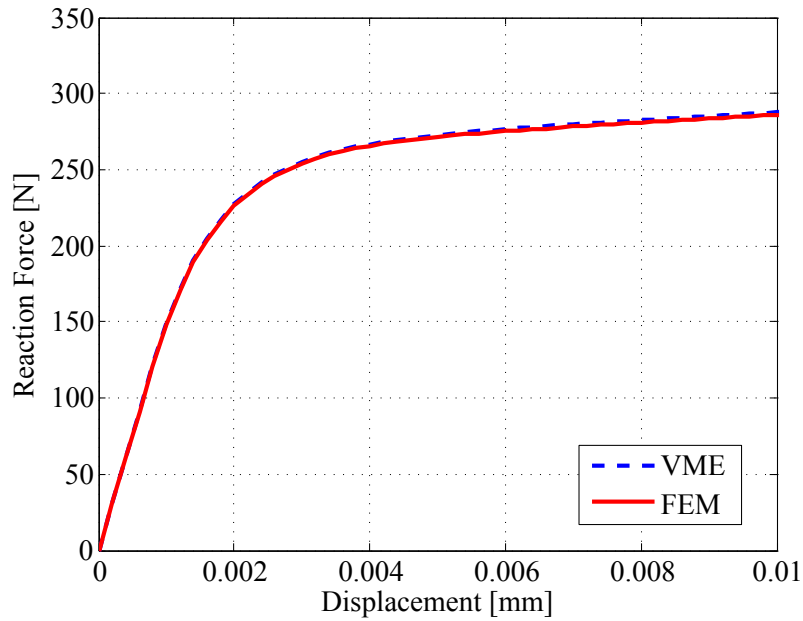


Figure 10: Overall reaction force - displacement comparison between the reference simulation and the VME method.

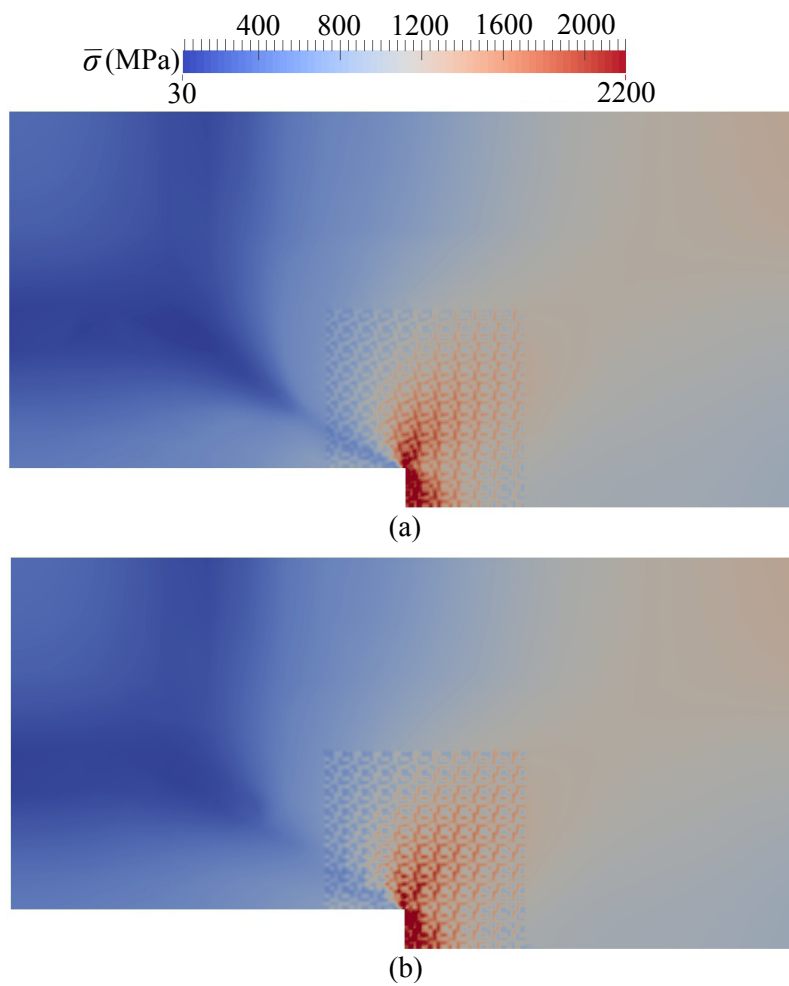


Figure 11: Comparison of equivalent stress contours at the end of the simulation:
 (a) reference model; and (b) the VME method with $\kappa = 2.96 \times 10^8$.

6 Conclusions and further research

This manuscript presented the extension of the variational multiscale enrichment (VME) method to account for the presence of material nonlinearity. The performance of a family of mixed boundary conditions is assessed in the nonlinear regime. The mixed boundary conditions reduce the overconstraint imposed by the homogeneous Dirichlet boundary conditions typically employed in the variational multiscale literature. The proposed computational formulation is advantageous in solving global-local problems, in which the solution accuracy is particularly important in a problem subdomain and within which the underlying material heterogeneities need to be resolved. The assessment study performed in this manuscript points to very high accuracy of the proposed computational methodology compared to direct numerical simulations. This implies that within the subdomain of interest, the local fields are accurately captured.

From the computational perspective, several key issues remain to be addressed, particularly related to the computational performance. The cost of the VME approach is on the same order as the domain decomposition approach. Similar to the domain decomposition, the proposed approach lends itself very well for large parallel implementations. The implementation strategy outlined in this paper is serial and an extension to parallel implementation is natural. Even on parallel processes, the direct evaluation of the enrichment domain problems could often be computationally challenging. The classical projection algorithms used in the variational multiscale literature may not lead to accurate local fields when the underlying microstructural heterogeneities are resolved. Nevertheless, reduced order microstructure evaluation algorithms (e.g., [32, 7]), which eliminate the need to evaluate full resolution boundary value problems at the enrichment region without significant loss of accuracy in capturing the local response fields, is critical to the practical application of the VME method. The extension of the proposed approach to the failure regime also remains outstanding. The accuracy of the VME approach starts to degrade if failure is introduced within the material microstructure. In multiscale problems, the solution accuracy in the failure regime is known to be significantly affected by the microstructural boundary conditions and appropriate boundary conditions need to be devised to retain high accuracy of the VME approach in the damage propagation regime. In its current state, the proposed VME approach is able to accurately characterize failure initiation. The above mentioned issues will be addressed in the near future.

7 Acknowledgements

The authors gratefully acknowledge the research funding from the Air Force Office of Scientific Research Multi-Scale Structural Mechanics and Prognosis Program (Grant No: FA9550-13-1-

0104. Program Manager: Dr. David Stargel). We also acknowledge the technical cooperation with Dr. Ravinder Chona and Dr. Ravi Penmetsa at the Air Force Research Laboratory, Structural Sciences Center.

References

- [1] T. Arbogast. Implementation of a locally conservative numerical subgrid upscaling scheme for two-phase Darcy flow. *Comput. GeoSci.*, 6:453–481, 2002.
- [2] T. Arbogast. Analysis of a two-scalecalecalecale, locally conservative subgrid upscaling for elliptic problems. *SIAM J. on Numer. Anal.*, 42:576, 2004.
- [3] C. Baiocchi, F. Brezzi, and L. P. Franca. Virtual bubbles and the galerkin-least-squares method. *Comput. Meth. Appl. Mech. Engrg.*, 105:125–142, 1993.
- [4] L. Berger-Vergiat, H. Waisman, B. Hiriyyur, R. Tuminaro, and D. Keyes. Inexact schwarz-algebraic multigrid preconditioners for crack problems modeled by extended finite element methods. *Int. J. Numer. Meth. Engrg.*, 90:311–328, 2012.
- [5] F. Brezzi, L. P. Franca, T. J. R. Hughes, and A. Russo. $b = \int g$. *Comput. Meth. Appl. Mech. Engrg.*, 145:329–339, 1997.
- [6] E. W. C. Coenen, V. G. Kouznetsova, and M. G. D Geers. Novel boundary conditions for strain localization analyses in microstructural volume elements. *Int. J. Numer. Meth. Engrg.*, 90:1–21, 2012.
- [7] R. Crouch and C. Oskay. Symmetric meso-mechanical model for failure analysis of heterogeneous materials. *Int. J. Solids Struct.*, 8:447–461, 2010.
- [8] C. A. Duarte and D. J. Kim. Analysis and applications of a generalized finite element method with global–local enrichment functions. *Comput. Meth. Appl. Mech. Engrg.*, 197:487–504, 2008.
- [9] J. Fish. The s-version of the finite element method. *Computers & Structures*, 43:539–547, 1992.
- [10] J. Fish and S. Markolefas. Adaptive global-local refinement strategy based on the interior error estimates of the h-method. *Int. J. Numer. Meth. Engrg.*, 37:827–838, 1994.
- [11] K. Garikipati. Variational multiscale methods to embed the macromechanical continuum formulation with fine-scale strain gradient theories. *Int. J. Numer. Meth. Engrg.*, 57:1283–1298, 2003.

- [12] K. Garikipati and T. J. R. Hughes. A study of strain localization in a multiple scale framework- the one-dimensional problem. *Comput. Meth. Appl. Mech. Engrg.*, 159:193–222, 1998.
- [13] K. Garikipati and T. J. R. Hughes. A variational multiscale approach to strain localization formulation for multidimensional problems. *Comput. Meth. Appl. Mech. Engrg.*, 188:39–60, 2000.
- [14] L. Gendre, O. Allix, P. Gosselet, and F. Comte. Non-intrusive and exact global/local techniques for structural problems with local plasticity. *Comput. Mech.*, 44:233–245, 2009.
- [15] S. Ghosh and D. Paquet. Adaptive concurrent multi-level model for multi-scale analysis of ductile fracture in heterogeneous aluminum alloys. *Mech. Mater.*, 65:12–34, 2013.
- [16] B. Hiriyur, R.S. Tuminaro, H. Waisman, E.G. Boman, and D.E. Keyes. A quasi-algebraic multigrid approach to fracture problems based on extended finite elements. *SIAM J. Sci. Comput.*, 34:A603–A626, 2012.
- [17] T. J. R. Hughes. Multiscale phenomena: Green’s functions, the dirichlet-to-neumann formulation, subgrid-scale models, bubbles and the origins of stabilized methods. *Comput. Meth. Appl. Mech. Engrg.*, 127:387–401, 1995.
- [18] T. J. R. Hughes and G. Sangalli. Variational multiscale analysis: the fine-scale green’s function, projection, optimization, localization, and stabilized methods. *SIAM J. Numer. Anal.*, 45:539–557, 2007. ISSN 00361429.
- [19] T. J. R. Hughes, G. R. Feijoo, and J. B. Quincy. The variational multiscale method - a paradigm for computational mechanics. *Comput. Meth. Appl. Mech. Engrg.*, 166:3–24, 1998.
- [20] A. Hund and E. Ramm. Locality constraints within multiscale model for non-linear material behaviour. *Int. J. Numer. Meth. Engrg.*, 70:1613–1632, 2007.
- [21] R. Juanes and F.-X. Dub. A locally conservative variational multiscale method for the simulation of porous media flow with multiscale source terms. *Comput. Geosci.*, 12:273–295, 2008.
- [22] H. P. Langtangen. *Computational partial differential equations: Numerical methods and diffpack programming*. Springer, 2003.

- [23] O. Lloberas-Valls, D. J. Rixen, A. Simone, and L. J. Sluys. Domain decomposition techniques for the efficient modeling of brittle heterogeneous materials. *Comput. Methods Appl. Mech. Engrg.*, 200:1577–1590, 2011.
- [24] K. M. Mao and C. T. Sun. A refined global-local finite element analysis method. *Int. J. Numer. Meth. Engng.*, 32:29–43, 1991.
- [25] D. Markovic and A. Ibrahimbegovic. On micro-macro interface conditions for micro scale based fem for inelastic behavior of heterogeneous materials. *Comput. Methods Appl. Mech. Engrg.*, 193:5503–5523, 2004.
- [26] A. Masud and K. Xia. A variational multiscale method for inelasticity: Application to superelasticity in shape memory alloys. *Comput. Methods Appl. Mech. Engrg.*, 195:4512–4531, 2006.
- [27] J. Mergheim. A variational multiscale method to model crack propagation at finite strains. *Int. J. Numer. Meth. Engng.*, 80:269–289, 2009.
- [28] C. D. Mote. Global-local finite element. *Int. J. Numer. Meth. Engng.*, 3:565–574, 1971.
- [29] A. K. Noor. Global-local methodologies and their application to nonlinear analysis. *Finite Elements Anal. Des.*, 2:333–346, 1986.
- [30] C. Oskay. Variational multiscale enrichment for modeling coupled mechano-diffusion problems. *Int. J. Numer. Meth. Engng.*, 89:686–705, 2012.
- [31] C. Oskay. Variational multiscale enrichment method with mixed boundary conditions for modeling diffusion and deformation problems. *Comput. Methods Appl. Mech. Engrg.*, 264:178–190, 2013.
- [32] C. Oskay and J. Fish. Eigendeformation-based reduced order homogenization for failure analysis of heterogeneous materials. *Comput. Methods Appl. Mech. Engrg.*, 196:1216–1243, 2007.
- [33] C. Oskay and M. Haney. Computational modeling of titanium structures subjected to thermo-chemo-mechanical environment. *Int. J. Solids Struct.*, 47:3341–3351, 2010.
- [34] D. Qian, G.J. Wagner, and W.K. Liu. A multiscale projection method for the analysis of carbon nanotubes. *Comput. Methods Appl. Mech. Engrg.*, 193:1603–1632, 2004.
- [35] H. Waisman and L. Berger-Vergiat. An adaptive domain decomposition preconditioner for crack propagation problems modeled by xfem. *Int. J. Mult. Comp. Eng.*, 2013:633–654, 2013.

- [36] H. Yan and C. Oskay. A three-field (displacement-pressure-concentration) formulation for coupled transport-deformation problems. *Finite Elements Anal. Des.*, 90:20–30, 2014.
- [37] H. Yan and C. Oskay. A viscoelastic-viscoplastic model of titanium structures subjected to thermo-chemo-mechanical environment. *Int. J. Solids Struct.*, 56-57:29–42, 2015.
- [38] J. Yeon and S. Youn. Variational multiscale analysis of elastoplastic deformation using meshfree approximation. *Int. J. Solids Struct.*, 45:4709–4724, 2008.

A Appendix

This appendix section presents the details of $\mathbf{C} = \left(\frac{\partial \dot{\boldsymbol{\varepsilon}}^{vp}}{\partial \boldsymbol{\sigma}}\right)$ and $\mathbf{G} = \left(\frac{\partial \dot{\boldsymbol{\varepsilon}}^{vp}}{\partial \boldsymbol{\varepsilon}^{vp}}\right)$ that are illustrated in Section 4.1. For the clarity of presentation, the bold symbol in this section denotes vector notation. Recall the evolution of plastic strain (Eq. (5)), the loading function (Eq. (6)) and the flow stress (Eq. (8)). Define

$$F \equiv \frac{f(\boldsymbol{\sigma}, \boldsymbol{\varepsilon}^{vp})}{\sigma_y(\boldsymbol{\varepsilon}^{vp})} \quad (60)$$

and

$$\mathbf{a} \equiv \frac{\partial f(\boldsymbol{\sigma}, \boldsymbol{\varepsilon}^{vp})}{\partial \boldsymbol{\sigma}} = \sqrt{3} \frac{\partial \bar{\sigma}}{\partial \boldsymbol{\sigma}} = \frac{\sqrt{3}}{2\bar{\sigma}} \tilde{\boldsymbol{\sigma}} \quad (61)$$

where, in 3D case $\tilde{\boldsymbol{\sigma}}$ is expressed in a vector format as:

$$\tilde{\boldsymbol{\sigma}} = \{s_{xx}, s_{yy}, s_{zz}, 2\sigma_{xy}, 2\sigma_{yz}, 2\sigma_{zx}\}^T \quad (62)$$

in which s denotes deviatoric stress components. Consequently, the plastic strain evolution equation is expressed as:

$$\dot{\boldsymbol{\varepsilon}}^{vp} = \gamma \langle F \rangle^q \mathbf{a} \quad (63)$$

and \mathbf{C} becomes:

$$\begin{aligned} \mathbf{C} &= \left(\frac{\partial \dot{\boldsymbol{\varepsilon}}^{vp}}{\partial \boldsymbol{\sigma}}\right) = \gamma \left[\langle F \rangle^q \frac{\partial \mathbf{a}}{\partial \boldsymbol{\sigma}} + q \langle F \rangle^{q-1} \frac{\partial \langle F \rangle}{\partial f} \frac{\partial f}{\partial \boldsymbol{\sigma}} \otimes \mathbf{a} \right] \\ &= \gamma \langle F \rangle^q \left[\frac{\partial \mathbf{a}}{\partial \boldsymbol{\sigma}} + \frac{q [\text{sign}(F) + 1]}{2 \langle f \rangle} \mathbf{a} \otimes \mathbf{a} \right] \end{aligned} \quad (64)$$

From Eq. (61):

$$\frac{\partial \mathbf{a}}{\partial \boldsymbol{\sigma}} = \frac{\sqrt{3}}{2\bar{\sigma}} \mathbf{M} - \frac{\sqrt{3}}{3\bar{\sigma}} \mathbf{a} \otimes \mathbf{a}; \quad \mathbf{M} = \frac{\partial \tilde{\boldsymbol{\sigma}}}{\partial \boldsymbol{\sigma}} \quad (65)$$

In 3D case, \mathbf{M} is expressed as:

$$\mathbf{M} = \begin{bmatrix} \frac{2}{3} & -\frac{1}{3} & -\frac{1}{3} & 0 & 0 & 0 \\ -\frac{1}{3} & \frac{2}{3} & -\frac{1}{3} & 0 & 0 & 0 \\ -\frac{1}{3} & -\frac{1}{3} & \frac{2}{3} & 0 & 0 & 0 \\ 0 & 0 & 0 & 2 & 0 & 0 \\ 0 & 0 & 0 & 0 & 2 & 0 \\ 0 & 0 & 0 & 0 & 0 & 2 \end{bmatrix} \quad (66)$$

Employing, \mathbf{M} , \mathbf{C} is written as:

$$\mathbf{C} = \gamma \langle F \rangle^q \left[\frac{\sqrt{3}}{2\bar{\sigma}} \mathbf{M} + \left(\frac{q [\text{sign}(F) + 1]}{2 \langle f \rangle} - \frac{\sqrt{3}}{3\bar{\sigma}} \right) \mathbf{a} \otimes \mathbf{a} \right] \quad (67)$$

Using Eq. (63):

$$\mathbf{G} = \frac{\partial \dot{\boldsymbol{\varepsilon}}^{vp}}{\partial \boldsymbol{\varepsilon}^{vp}} = \frac{\gamma q}{2} \langle F \rangle^{q-1} [\text{sign}(F) + 1] \frac{\partial F}{\partial \boldsymbol{\varepsilon}^{vp}} \otimes \mathbf{a} \quad (68)$$

Employing chain rule, we obtain:

$$\frac{\partial F}{\partial \boldsymbol{\varepsilon}^{vp}} = \frac{\partial f}{\partial \bar{\boldsymbol{\varepsilon}}^{vp}} \frac{\partial \bar{\boldsymbol{\varepsilon}}^{vp}}{\partial \boldsymbol{\varepsilon}^{vp}} \frac{1}{\sigma_y} - \frac{f}{\sigma_y^2} \frac{\partial \sigma_y}{\partial \bar{\boldsymbol{\varepsilon}}^{vp}} \frac{\partial \bar{\boldsymbol{\varepsilon}}^{vp}}{\partial \boldsymbol{\varepsilon}^{vp}} = -\frac{2}{3} B n (\bar{\boldsymbol{\varepsilon}}^{vp})^{n-2} \left(\frac{\sigma_y + f}{\sigma_y^2} \right) \boldsymbol{\varepsilon}^{vp} \quad (69)$$

Therefore,

$$\mathbf{G} = -[\text{sign}(F) + 1] \left(\frac{\gamma q B n}{3} \right) \langle F \rangle^{q-1} (\bar{\boldsymbol{\varepsilon}}^{vp})^{n-2} \left(\frac{\sqrt{3}\bar{\sigma}}{\sigma_y^2} \right) \boldsymbol{\varepsilon}^{vp} \otimes \mathbf{a} \quad (70)$$